

AD-A110 365

AIR FORCE INST OF TECH WRIGHT-PATTERSON AFB OH

F/G A/2

DIGITAL METEOROLOGICAL RADAR DATA COMPARED WITH DIGITAL INFRARE--ETC(U)

MAY 79 R S HENDERSON

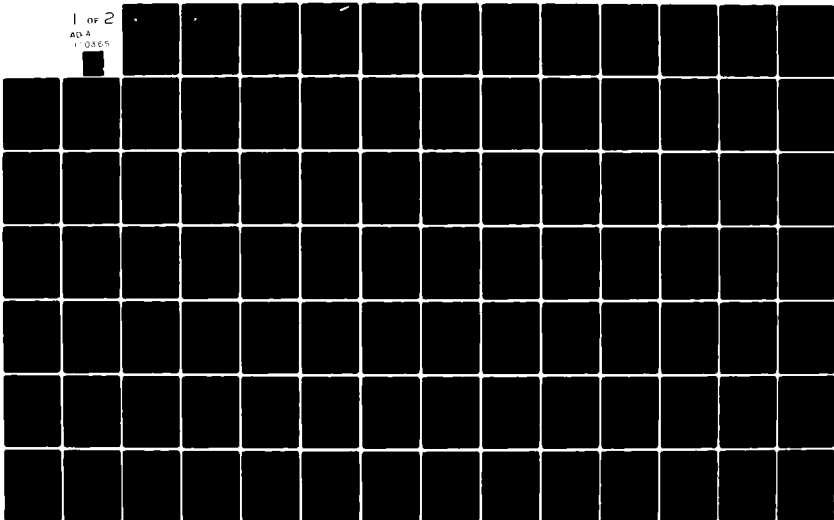
AFIT-CI-79-278T-5

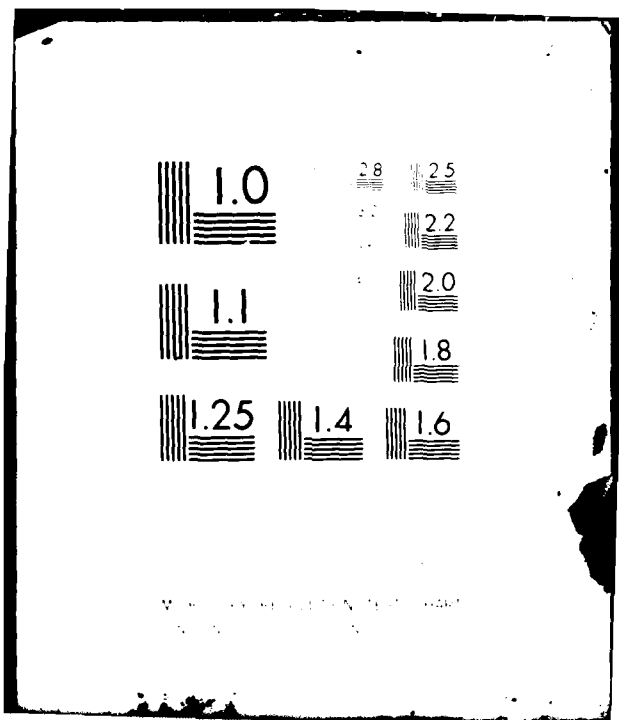
NL

UNCLASSIFIED

1 of 2

AD-A
170465

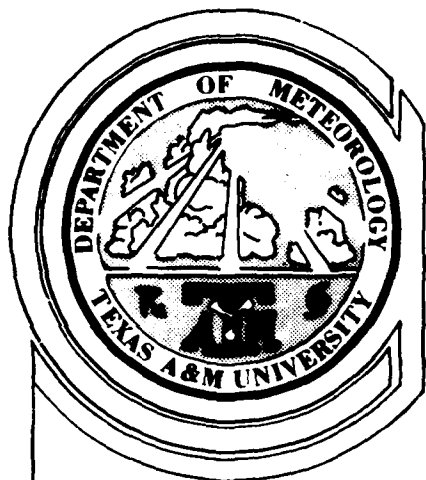




Resolution Test Chart
1963

79-278T-S

LEVEL II



TEXAS A&M UNIVERSITY

DEPARTMENT OF
METEOROLOGY

AD A110365

DIGITAL METEOROLOGICAL RADAR DATA COMPARED
WITH DIGITAL INFRARED DATA FROM A
GEOSTATIONARY METEOROLOGICAL SATELLITE

by

Rodney S. Henderson

May 1979

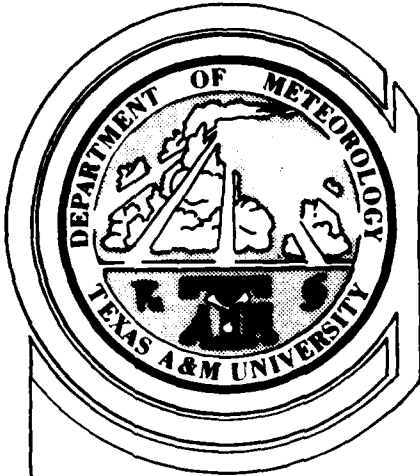
DTIC
ELECTE
FEB 3 1982
S D D

DTIC FILE COPY

DISTRIBUTION STATEMENT A

Approved for public release;
Distribution Unlimited





TEXAS A & M UNIVERSITY

DEPARTMENT OF METEOROLOGY

DIGITAL METEOROLOGICAL RADAR DATA COMPARED
WITH DIGITAL INFRARED DATA FROM A
GEOSTATIONARY METEOROLOGICAL SATELLITE

by

Rodney S. Henderson

May 1979

Accession For	
NTIS GRA&I	<input checked="" type="checkbox"/>
DTIC TAB	<input type="checkbox"/>
Unannounced	<input type="checkbox"/>
Justification	
By	
Distribution/	
Availability Codes	
Dist	Avail and/or Special
A	



DTIC
ELECTE
S FEB 3 1982 D
D

DISTRIBUTION STATEMENT A

Approved for public release;
Distribution Unlimited



UNCLASS

SECURITY CLASSIFICATION OF THIS PAGE (When Data Entered)

AFIT- REPORT DOCUMENTATION PAGE		READ INSTRUCTIONS BEFORE COMPLETING FORM
1. REPORT NUMBER 79-278T-S	2. GOVT ACCESSION NO. AD-8990365	3. REPORTS CATALOG NUMBER
4. TITLE (and Subtitle) Digital Meteorological Radar Data Compared With Digital Infrared Data From a Geostationary Meteorological Satellite		5. TYPE OF REPORT & PERIOD COVERED THESIS/DISSERTATION
7. AUTHOR(s) Capt Rodney Stuart Henderson		6. PERFORMING ORG. REPORT NUMBER
9. PERFORMING ORGANIZATION NAME AND ADDRESS AFIT STUDENT AT: Texas A&M University		8. CONTRACT OR GRANT NUMBER(s)
11. CONTROLLING OFFICE NAME AND ADDRESS AFIT/NR WPAFB OH 45433		10. PROGRAM ELEMENT PROJECT TASK AREA & WORK UNIT NUMBERS
14. MONITORING AGENCY NAME & ADDRESS (if different from Controlling Office)		12. REPORT DATE May 1979
		13. NUMBER OF PAGES 116
		15. SECURITY CLASS (of this report) UNCLASS
		15a. DECLASSIFICATION/DOWNGRADING SCHEDULE
16. DISTRIBUTION STATEMENT (of this Report) APPROVED FOR PUBLIC RELEASE; DISTRIBUTION UNLIMITED		
17. DISTRIBUTION STATEMENT (of the abstract entered in Block 20, if different from Report) 22 JAN 1982 <i>Fredric C. Lynch</i>		
18. SUPPLEMENTARY NOTES APPROVED FOR PUBLIC RELEASE: IAW AFR 190-17		FREDRIC C. LYNCH, Major, USAF Director of Public Affairs Air Force Institute of Technology (ATC) Wright-Patterson AFB, OH 45433
19. KEY WORDS (Continue on reverse side if necessary and identify by block number)		
20. ABSTRACT (Continue on reverse side if necessary and identify by block number) ATTACHED 82 02 01 085		


R
I
N
T

TEXAS A&M UNIVERSITY

COLLEGE OF GEOSCIENCES

COLLEGE STATION, TEXAS 77843

23 April 1979


79-278T-S

Reply to
Department of
METEOROLOGY/Capt Henderson
Telephone (713) 845-6011

AFIT/CIRF
Wright-Patterson AFB

The following information is submitted as required by AFITR
53-1:

- a. Author/Title: Rodney Stuart Henderson,
Digital Meteorological Radar Data Compared
With Digital Infrared Data From a Geostationary
Meteorological Satellite.
- b. Rank/Service: Capt, USAF.
- c. Year: 1979.
- d. Number of Pages: 116.
- e. Degree: M.S./Meteorology, Texas A&M University.
- f. Abstract:

Digital 10 cm radar data were collected using the Texas A&M University weather radar system. The digital radar data were then compared with GOES-East infrared imagery mapped to the digital radar grid projection. Point values of infrared digital count were correlated with point values of zero-tilt reflectivity, low-level PVSZ, mid-level PVSZ, upper-level PVSZ, and VIL for selected portions of two digital radar tilt-sequences. Correlations were also performed using thresholded infrared images and thresholded digital radar data.

The results indicated a positive correlation between infrared digital count and the digital radar data. Thresholding the infrared imagery was found to improve the correlation between infrared digital count and digital radar data. Thresholding the digital radar data produced less conclusive results.

- g. A list of key primary and secondary sources is attached.


RODNEY S. HENDERSON, Capt, USAF

Atch:
References.

Subject: Thesis Abstract.

REFERENCES

- Adler, R.F., and D.D. Fenn, 1977: Satellite-based thunderstorm intensity parameters. Preprints 10th Conf. on Severe Local Storms, Omaha, Amer. Meteor. Soc., 8-15.
- Blackmer, R.H., Jr., 1961: Satellite observations of squall line thunderstorms. Proc. 9th Radar Meteor. Conf., Kansas City, Amer. Meteor. Soc., 76-82.
- , 1975: Correlation of cloud brightness and radiance with precipitation intensity. Tech. Rpt. NEPRF TR 8-75(SRI), Contract N66314-74-C-2350, Stanford Research Institute, 134 pp.
- , and S.M. Serebreny, 1968: Analysis of maritime precipitation using radar data and satellite cloud photographs. J. Appl. Meteor., 7, 122-131.
- Boucher, R.J., 1967: Relationships between the size of satellite-observed cirrus shields and the severity of thunderstorm complexes. J. Appl. Meteor., 6, 564-572.
- Cheng, N., and D. Rodenhuis, 1977: An intercomparison of satellite images and radar rainfall rates. Preprints 11th Technical Conf. on Hurricanes and Tropical Meteorology, Miami Beach, Amer. Meteor. Soc., 224-226.
- Fujita, T.T., 1977: Meteorological satellite observations and army operations. Tech. Rpt. ECOM 77-6, University of Chicago, 37 pp.
- Gerrish, H.P., 1970: Satellite and radar analysis of mesoscale features in the tropics. Tech. Rpt. ECOM-0205-F, University of Miami, 45 pp.
- , 1975: Satellite and radar analysis of mesoscale weather systems. Tech. Rpt. ECOM-0014-F, University of Miami, 34 pp.
- Griffith, C.G., and W.L. Woodley, 1973: On the variation with height of the top brightness of precipitating convective clouds. J. Appl. Meteor., 12, 1086-1089.
- , W.L. Woodley, P.G. Grube, D.W. Martin, J. Stout, and D.N. Sikdar, 1978: Rain estimation from geosynchronous satellite imagery - visible and infrared studies. Mon. Wea. Rev., 106, 1153-1171.
- Gruber, A., 1973: Estimating rainfall in regions of active convection. J. Appl. Meteor., 12, 110-118.

- Nagle, R.E., 1963: Comparisons of time integrated radar detected precipitation with satellite observed cloud patterns. Proc. 10th Radar Meteor. Conf., Washington, Amer. Meteor. Soc., 13-16.
- , and S.M. Serebreny, 1962: Radar precipitation echo and satellite cloud observations of a maritime cyclone. J. Appl. Meteor., 1, 279-295.
- Negri, A.J., D.W. Reynolds, and R.A. Maddox, 1976: Measurements of cumulonimbus clouds using quantitative satellite and radar data. Proc. 7th Conf. on Aerospace and Aeronautical Meteor. and Symp. on Remote Sensing from Satellites, Melbourne, Amer. Meteor. Soc., 119-124.
- Phillips, J.F., 1975: Cloud structures from Defense Meteorological Satellite data. M.S. thesis, Texas A&M University, 142 pp.
- Reynolds, D.W., 1978: An intensive analysis of digital radar, raingage, and digital satellite data for a convective cloud system on the High Plains of Montana. Preprints 4th Symp. on Meteorological Observations and Instrumentation, Denver, Amer. Meteor. Soc., 310-317.
- , and T.H. Vonder Haar, 1973: A comparison of radar-determined cloud height and reflected solar radiance measured from the geosynchronous satellite ATS-3. J. Appl. Meteor., 12, 1082-1085.
- , T.H. Vonder Haar, and L.O. Grant, 1978: Meteorological satellites in support of weather modification. Bull. Amer. Meteor. Soc., 59, 269-281.
- Sieland, T.E., 1977: Real-time computer techniques in the detection and analysis of severe storms from digital radar data. Ph.D. dissertation, Texas A&M University, 141 pp.
- Sikdar, D.N., 1972: ATS-3 observed cloud brightness field related to a meso-synoptic scale rainfall pattern. Tellus, 24, 400-413.
- Smith, E.A., and D.W. Reynolds, 1978: The generation and display of digital radar-satellite composites using analytic mapping techniques and solid state video refresh technology. Preprints Conf. on Wea. Forecasting and Analysis and Aviation Meteor., Silver Spring, Amer. Meteor. Soc., 201-205.
- Vonder Haar, T.H., 1969: Meteorological applications of reflected radiance measurements from ATS 1 and ATS 3. J. Geophys. Res., 74, 5404-5412.

_____, and R.S. Cram, 1970: A pilot study on the application of geosynchronous meteorological satellite data to very short range terminal forecasting. Tech. Rpt. AFCRL 70-0493, Space Science and Engineering Center, University of Wisconsin, 116 pp.

Wexler, R., and L.J. Allison, 1972: Radar and Nimbus IV infrared measurements of the Oklahoma City tornadoes, 30 April 1970. Preprints 15th Radar Meteor. Conf., Champaign-Urbana, Amer. Meteor. Soc., 77-82.

DIGITAL METEOROLOGICAL RADAR DATA COMPARED
WITH DIGITAL INFRARED DATA FROM A
GEOSTATIONARY METEOROLOGICAL SATELLITE

A Thesis

by

RODNEY STUART HENDERSON

Submitted to the Graduate College of
Texas A&M University
in partial fulfillment of the requirement for the degree of

MASTER OF SCIENCE

May 1979

Major Subject: Meteorology

DIGITAL METEOROLOGICAL RADAR DATA COMPARED
WITH DIGITAL INFRARED DATA FROM A
GEOSTATIONARY METEOROLOGICAL SATELLITE

A Thesis

by

RODNEY STUART HENDERSON

Approved as to style and content by:

George L. Hubner
(Chairman of Committee)

Raymond W. Thompson
(Member)

Vance Meyer
(Member)

Alvin Williams
(Member)

K.C. Brundage
(Head of Department)

May 1979

ABSTRACT

Digital Meteorological Radar Data Compared with
Digital Infrared Data from a Geostationary
Meteorological Satellite. (May 1979)

Rodney Stuart Henderson, B.A.E.,
Georgia Institute of Technology

Chairman of Advisory Committee: Dr. George Huebner

↓
Digital 10 cm radar data were collected using the Texas A&M University weather radar system. The digital radar data were then compared with GOES-East infrared imagery mapped to the digital radar grid projection. Point values of infrared digital count were correlated with point values of zero-tilt reflectivity, low-level PVSZ, mid-level PVSZ, upper-level PVSZ, and VIL for selected portions of two digital radar tilt-sequences. Correlations also were performed using thresholded infrared images and thresholded digital radar data.

The results indicated a positive correlation between infrared digital count and the digital radar data. Thresholding the infrared imagery was found to improve the correlation between infrared digital count and digital radar data. Thresholding the digital radar data produced less conclusive results.

∩

ACKNOWLEDGMENTS

The author's graduate program was sponsored and financed by the Air Force Institute of Technology, United States Air Force.

I wish to express sincere appreciation to the following individuals whose guidance and assistance have made this endeavor possible:

Dr. George Huebner, my committee chairman, for his encouragement, advice, and support throughout this program.

Dr. Aylmer Thompson, for serving patiently on my committee and for his many contributions to the development of this study.

Dr. Vance Moyer, for serving on my committee and for his support and assistance in developing this manuscript and others.

Dr. Glen Williams, for serving on my committee and reviewing this manuscript.

Mr. J. T. Young of the Space Science and Engineering Center, University of Wisconsin, for providing the satellite data and advice regarding its use.

Mr. Ray McAnelly, for his generation of the digital radar data used in this study.

Mr. T. O. Haig, also of the Space Science and Engineering Center, for information on the McIDAS system.

Mrs. Jane Kraft for her patience and efforts in typing this
manuscript.

DEDICATION

To my wife, Sandra, whose patience and understanding have made this thesis possible, and to my sons, Bryan and Jeremy, for their support and encouragement.

TABLE OF CONTENTS

	Page
ABSTRACT	iii
ACKNOWLEDGMENTS	iv
DEDICATION	vi
TABLE OF CONTENTS	vii
LIST OF TABLES	ix
LIST OF FIGURES	x
LIST OF ACRONYMS	xii
CHAPTER	
I. INTRODUCTION	1
1. The Need for This Investigation	1
2. Present Status of Research Relating to This Investigation	3
3. Objectives of the Investigation	7
4. Techniques and Scope of the Investigation	8
II. METEOROLOGICAL RADAR DATA	10
1. Basic Radar Theory	10
2. Earth Curvature Correction	13
3. The TAMU Weather Radar System	15
4. Data Reduction and Display	17
III. GEOSTATIONARY METEOROLOGICAL SATELLITE DATA	20
1. The SMS/GOES Spacecraft	20
2. The Visible and Infrared Spin Scan Radiometer	22
3. Data Distribution and Processing	23

TABLE OF CONTENTS (Continued)

CHAPTER	Page
4. Basic Characteristics of Infrared Satellite Data	26
5. McIDAS Data	27
6. Data Reduction and Display	29
 IV. COMPARISON OF DIGITAL RADAR AND SATELLITE DATA	 38
1. The Basis for the Comparison	38
2. First Tilt-sequence and Corresponding GOES Images	40
3. Tenth Tilt-sequence and Corresponding GOES Images	50
4. Correlations Between the Radar and Satellite Data	66
5. The Effect of Thresholding the Data	71
 V. CONCLUSIONS AND RECOMMENDATIONS	 83
1. Conclusions	83
2. Recommendations	86
 REFERENCES	 90
 APPENDIX A	 94
 VITA	 103

LIST OF TABLES

TABLE		Page
1	Displacement corrections for cloud height.	36
2	Displacement correction for each image	37
3	Values of r and p for the first tilt-sequence and corresponding GOES images	68
4	Values of r and p for the tenth tilt-sequence and corresponding GOES images (southwest sector)	70
5	Values of r and p for the tenth tilt-sequence and corresponding GOES images (northwest sector)	72
6	MB enhancement (after Corbell <u>et al.</u> , 1976)	75
7	Values of r and p for the first tilt-sequence and thresholded GOES images	77
8	Values of r and p for thresholded radar data and GOES images	80

LIST OF FIGURES

FIGURE		Page
1	SMS/GOES Data Distribution.	25
2	Navigated points and mapping to the digital radar grid	32
3	Tilt-sequence one, zero-tilt reflectivity (dBZ)	41
4	Tilt-sequence one, low-level PVSZ (dBZ)	42
5	Tilt-sequence one, mid-level PVSZ (dBZ)	43
6	Tilt-sequence one, upper-level PVSZ (dBZ)	44
7	Tilt-sequence one, VIL (kg m^{-2})	45
8	0015 GMT, 3 May 1978 infrared image.	46
9	0030 GMT, 3 May 1978 infrared image.	47
10	GOES infrared digital count to temperature calibration.	48
11	Tilt-sequence ten, southwest sector, zero-tilt reflectivity (dBZ)	51
12	Tilt-sequence ten, southwest sector, low-level PVSZ (dBZ)	52
13	Tilt-sequence ten, southwest sector, mid-level PVSZ (dBZ)	53
14	Tilt-sequence ten, southwest sector, upper-level PVSZ (dBZ)	54

LIST OF FIGURES (Continued)

FIGURE		Page
15	Tilt-sequence ten, southwest sector, VIL (kg m^{-2}).	55
16	0215 GMT, 3 May 1978 infrared image, southwest sector	56
17	0230 GMT, 3 May 1978 infrared image, southwest sector	57
18	Tilt-sequence ten, northwest sector, zero-tilt reflectivity (dBZ)	58
19	Tilt-sequence ten, northwest sector, low-level PVSZ (dBZ)	59
20	Tilt-sequence ten, northwest sector, mid-level PVSZ (dBZ)	60
21	Tilt-sequence ten, northwest sector, upper-level PVSZ (dBZ)	61
22	Tilt-sequence ten, northwest sector, VIL (kg m^{-2}).	62
23	0215 GMT, 3 May 1978 infrared image, northwest sector	63
24	0230 GMT, 3 May 1978 infrared image, northwest sector	64
25	MB enhancement curve (after Corbell, <u>et al.</u> , 1976).	74

LIST OF ACRONYMS

AOIFS	Atmospheric and Oceanic Information Processing System
ATS	Applications Technology Satellite
CDA	Command and Data Acquisition station
CDDF	Central Data Distribution Facility
DMSP	Defense Meteorological Satellite Program
DVIP	digital video integrator and processor
ESSA	Environmental Science Services Administration
GMT	Greenwich Mean Time
GOES	Geostationary Operational Environmental Satellite
McIDAS	Man-computer Interactive Data Access System
NESS	National Environmental Satellite Service
NOAA	National Oceanic and Atmospheric Administration
NSSL	National Severe Storms Laboratory
PPI	plan position indicator
PVSZ	partial vertically-summed reflectivity
SAS 76	Statistical Analysis System 76
SEM	Space Environmental Monitor
SFSS	Satellite Field Service Station
SMS	Synchronous Meteorological Satellite
SSEC	Space Science and Engineering Center

LIST OF ACRONYMS (Continued)

TAMU	Texas A&M University
TIROS	Television and Infrared Observation Satellite
TTC	Telemetry, Tracking, and Command
VIL	vertically-integrated liquid water content
VISSR	visible and infrared spin scan radiometer

CHAPTER I

INTRODUCTION

The importance and use of weather radar as a means of detecting, observing, and forecasting severe weather phenomena is firmly established. Meteorological satellite data, particularly data from geostationary satellites, have also proved to be of great value in detecting, observing, and forecasting severe weather phenomena. The increasing availability of digital data from both meteorological radars and geostationary satellites makes ready comparison of both types of data feasible and useful in the analysis of severe weather phenomena. The possibility that characteristics of severe weather phenomena shared in common by the two types of data can be used in the real-time analysis and forecasting of severe weather has made comparisons of these data attractive to both operational and research meteorologists.

1. The Need for This Investigation

The increasing automation of systems for handling large volumes of meteorological data and the proliferation of interactive systems

The citations on the following pages follow the style of the Journal of Applied Meteorology.

designed to display and compare fields of satellite, digital radar, and conventional surface and upper-air data have focused increased interest on the development of procedures to acquire and analyze such data on a real-time basis for the forecasting of severe weather development. Interactive meteorological data handling systems are in use at some universities and within government agencies charged with research and development responsibilities. Interactive systems are expected to be in use at selected central forecasting facilities within the National Weather Service and the Air Weather Service in the near future. These systems must allow for rapid analysis of all data fields and ready comparison of significant features in each field of data with features in the other data fields. Maximizing the usefulness of such systems in forecasting applications also requires an understanding of the significant relationships between data fields such as digital satellite data and digital radar data. The large volume of high resolution digital data available at frequent intervals from the geostationary satellites such as the GOES (Geostationary Operational Environmental Satellite) spacecraft suggests that significant relationships may be established between the satellite data and simultaneous digital radar data which may be useful in the development of rainfall and flood forecasting techniques.

2. Present Status of Research Relating to This Investigation

Comparisons of meteorological satellite imagery with radar data have generally been either of a qualitative or a quantitative nature. Qualitative comparisons began shortly after the launch of TIROS 1 (Television and Infrared Observation Satellite 1), the world's first full-time meteorological satellite. Blackmer (1961) and Nagle (1963) used TIROS 1 imagery in comparison with available radar precipitation patterns to study squall line activity. Nagle and Serebreny (1962) compared TIROS 1 imagery with scope photographs from ground-based and airborne radars in studying the precipitation patterns associated with a maritime cyclone. Boucher (1967) compared imagery from several TIROS spacecraft with available radar data and mesoscale analyses in examining the relationship of satellite-observed cirrus shields to the severity of thunderstorm systems. Boucher found that the diameter of the cirrus shield resulting from the integration of all anvil clouds within a thunderstorm complex was an indicator of storm severity. Blackmer and Serebreny (1968) developed models of cloud and precipitation patterns associated with maritime cyclones based on TIROS 9 imagery, shipborne and shore-based radar data, and surface and upper-air data.

Vonder Haar (1969) employed data from the geostationary satellites ATS 1 (Applications Technology Satellite 1) and ATS 3 in a study

of reflected radiance applications which presented a detailed composite of a reflected radiance field and meteorological radar reports. Vonder Haar and Cram (1970) also used ATS 3 imagery in a short-range forecasting study which included radar data as well as surface observations within a mesonet network. SMS/GOES (Synchronous Meteorological Satellite/GOES) imagery, raingage data, and radar data provided the data base for Fujita's (1977) study of meteorological satellite applications for army operations.

Quantitative comparisons of meteorological radar and meteorological satellite data have been made using data from both polar-orbiting and geostationary satellites. Wexler and Allison (1972) employed Nimbus 4 infrared data and a reflectivity map from the National Severe Storms Laboratory (NSSL) WSR-57 radar to study a tornado outbreak that occurred near Oklahoma City. Gruber (1973) also used Nimbus 4 infrared data to determine areas of deep convection and compared his findings to radar data as part of a study concerned with estimating rainfall in convective areas.

ESSA 5 (Environmental Science Services Administration 5) and ESSA 7 satellite digital cloud mosaic films were examined by Gerrish (1970) to determine the cloudiness in each element of a grid array centered south of Miami, Florida. Gerrish used those data along with WSR-57 radar data, raingage data, and upper-air data in

examining the relationship between rainfall and cloudiness within the grid area. Gerrish (1975) later used DMSP (Defense Meteorological Satellite Program) satellite visible and infrared data and ATS 3 visible data in a similar study of cloudiness and precipitation. Gerrish determined that radar echo area correlated best with DMSP infrared cloud area at 18,000 ft and at 30,000 ft and that, on the average, radar echoes occupied only 42 per cent of the cloud area at those altitudes. DMSP data also were used by Phillips (1975) in a study that compared infrared satellite data with digital radar data from the NSSL. Phillips concluded that the DMSP imagery could be studied in greater detail when digitized using a microdensitometer but that detailed determination of the structure of convective storm activity did not seem possible with the infrared sensors then in use.

Blackmer (1975) studied the extent to which a combination of visible and infrared data indicated the presence and intensity of precipitation within a cloud and concluded that departures of brightness or radiance in small areas from the average value within the cloud cover over a large area could be used to infer precipitation. Cheng and Rodenhuis (1977) used NOAA 2 (National Oceanic and Atmospheric Administration 2) visible and infrared imagery along with WSR-57 radar data in comparing satellite images with radar rainfall rates. They found correlation coefficients between satellite data

and radar rainfall rates of from 0.23 to 0.34 for visible data and from 0.17 to 0.27 for infrared data.

Sikdar (1972) evaluated the relationship of rainfall patterns to cloud brightness fields and found that all of the radar echoes were included in the upper 36 to 40 per cent of the ATS 3 brightness range for the two cases considered. He indicated an excellent correlation between positive brightness anomaly area, radar echo area, and the precipitation pattern. Reynolds and Vonder Haar (1973) claimed that when growth of clouds could be detected by radar a corresponding increase in reflected radiance could be detected in ATS 3 visible imagery. Griffith and Woodley (1973) compared reflected radiances with radar-measured echo heights and found a positive correlation between cloud brightness and echo height. However, Negri *et al.* (1976) reported that brightness did not seem to correlate well with any echo parameters. Negri *et al.* also indicated that cloud area changes led echo area changes for the storm they examined. Adler and Fenn (1977) found that duration of cloud elements, minimum cloud-top temperature, and cold area rate of increase seemed to be correlated with the occurrence of severe weather.

Reynolds (1978) used an interactive computer system to evaluate digital radar and digital GOES data. Reynolds indicated that infrared

data show relative changes in top height which are related well to rainfall and that maximum rainfall occurs before the coldest cloud-top temperature is reached. Reynolds et al. (1978) also considered the use of meteorological satellites in weather modification projects and included comparisons of radar data and geostationary satellite data in seeking further to explore satellite-rainfall relationships. Smith and Reynolds (1978) have developed procedures to produce numerical composites of digital radar and digital satellite data for use in analyzing precipitation patterns.

Griffith et al. (1978) employed ATS 3 and SMS/GOES imagery in rainfall estimation applications using digital radar and rain gauge data for ground truth. They developed a rainfall estimation procedure based on the growth of radar echoes and satellite cloud areas and examined the procedure for potential real-time applications and automation.

3. Objectives of the Investigation

The primary objective of this investigation is to compare digital meteorological radar data with infrared imagery from a meteorological satellite in geostationary earth orbit by determining the correlation between point values of infrared digital count and point values of radar reflectivity and vertically integrated liquid water content (VIL). Comparisons are made between infrared digital count from the

satellite sensor and zero-tilt reflectivity, three levels of partial vertically-summed reflectivity (PVSZ), and VIL, for the purpose of determining which sets of data demonstrate the best relationship between the satellite and radar data.

A secondary objective of this investigation is to develop and implement procedures for computer processing of GOES imagery stored on magnetic tape and to map the data to points in the Texas A&M University (TAMU) digital weather radar grid.

4. Techniques and Scope of the Investigation

The radar data for this investigation were obtained from the digital weather radar system in the Department of Meteorology at TAMU. The reduction, interpolation and display of the radar data were accomplished on the Amdahl 470 V/6 computer at TAMU using the technique developed by Sieland (1977) as modified by McAnelly (1979). The digital GOES infrared data were obtained from the Man-computer Interactive Data Access System (McIDAS) at the Space Science and Engineering Center of the University of Wisconsin in Madison, Wisconsin. Reduction and display of the digital satellite data also were accomplished by the Amdahl 470 V/6 computer using a technique designed to map the satellite data to individual points in the radar grid established by the Sieland technique.

Tilt-sequence 10-cm digital radar data were collected near-simultaneously with GOES infrared imagery on 3 May 1978. The tilt-sequence data were processed to produce point values of zero-tilt reflectivity, three levels of partial vertically summed reflectivity (PVSZ), and vertically integrated liquid water content (VIL). The point values of the digital radar data were then tabulated along with GOES infrared digital count data mapped to corresponding points. The GOES infrared data were mapped from images at times corresponding to the start of the radar tilt-sequences and the end of the tilt-sequences. The tabulated data were punched onto computer cards and processed to compute correlations between each field of radar and satellite data.

Three sets of radar and satellite data were processed to reduce computer costs and meet time constraints imposed by tabulating the data and punching the data onto computer cards. One set of data was selected during the early development of radar echoes in the TAMU area and included one tilt-sequence of radar data and two infrared images for a corresponding area. The remaining two data sets were selected from a time when radar echo activity in the area appeared to be at or near its maximum intensity. The last two data sets were taken from a single tilt-sequence and from two corresponding infrared images.

CHAPTER II

METEOROLOGICAL RADAR DATA

Microwave radar is one of the many tools employed by meteorologists in studying the atmosphere. Digital radar systems have made possible quantitative comparisons of large volumes of radar data with data from other sources including the meteorological satellite data employed in this study. Much of the material in this chapter concerned with basic radar theory and the TAMU weather radar system is extracted from Neyland (1978) that contains a more complete description of the digital radar system and the Sicland (1977) computer program.

1. Basic Radar Theory

The basic form of the radar equation used by radar meteorologists was derived by Probert-Jones (1962). Probert-Jones assumed a more realistic beam shape than had been used in previous derivations and further assumed that no significant attenuation existed between the radar antenna and the target and that the target completely filled the spatial volume illuminated by the radar beam. With these assumptions, the average backscattered power, \bar{P}_r (watts), received from the target at range r (km), is given by

$$\bar{P}_r = \frac{c |k|^2}{r^2} Z_e \quad (1)$$

where c ($w \text{ km}^2 \text{ m}^3 \text{ mm}^{-6}$) is the radar constant unique to the individual radar, $|k|^2$ (dimensionless) is the dielectric constant from scattering theory, and Z_e ($\text{mm}^6 \text{ m}^{-3}$) is the equivalent radar reflectivity factor. An expression for the radar constant is given by

$$c = \frac{\pi^3 P_t G^2 h \theta \phi}{512 \lambda^2 2 \ln 2} \quad (2)$$

where P_t is the transmitted power during a radar pulse (w), G is the antenna gain (dimensionless), h is the pulse length in space of the transmitted pulse (cm), θ is the horizontal beamwidth (radians), ϕ is the vertical beamwidth (radians), and λ is the wavelength of the transmitted microwave energy (cm). The factor $2 \ln 2$ is the Probert-Jones correction factor. The value of c is 8.609×10^{-11} for the TAMU 10 cm radar and the value of $|k|^2$ is 0.93 (Battan, 1973).

The output of the radar system is digitized values of returned power, \bar{P}_r , which must be converted to values of reflectivity before further data reduction. The usual practice is to measure the returned power in terms of decibels with respect to a standard reference power level, normally 1 mw. Power levels are then expressed in units of dB_m , either above (+) or below (-) 1 mw according to

$$P(\text{dB}_m) = 10 \log_{10} \frac{P(\text{watts})}{10^{-3}(\text{watts})} \quad (3)$$

To determine values of Z_e , Eq. (1) is solved for Z_e giving

$$Z_e = \frac{r^2}{c |k|^2} \bar{P}_r . \quad (4)$$

Taking the logarithm of Eq. (4) gives

$$\log_{10}(Z_e) = 2 \log_{10} r + \log_{10} \bar{P}_r - \log_{10} c |k|^2 . \quad (5)$$

For the TAMU 10 cm radar, c is equal to 8.609×10^{-11} and $\log_{10} c |k|^2$ equals -10.1. Substituting these values into Eq. (5) gives

$$\log_{10} Z_e = 2 \log_{10} r + \log_{10} \bar{P}_r + 10.1 . \quad (6)$$

The digital value of \bar{P}_r is converted to its dBm equivalent (always negative) through the use of calibration data. The received power in watts is related to the received power in dBm by

$$\log_{10} \bar{P}_r \text{ (watts)} = 0.1 \bar{P}_r \text{ (dBm)} - 3.0 . \quad (7)$$

Substitution of Eq. (7) into Eq. (6) gives

$$\log_{10} Z_e = 0.1 \bar{P}_r + 2 \log_{10} r + 7.1 . \quad (8)$$

Finally, the value of Z_e is given by

$$Z_e = 10^{(0.1 \bar{P}_r + 2 \log_{10} r + w_c)} \quad (9)$$

where Z_e is in units of $\text{mm}^6 \text{ m}^{-3}$ and w_c is 7.1.

The several assumptions inherent in the development of Eq. (9) include:

- 1) The transmitted microwave energy is not significantly

attenuated between the radar antenna and the target. This assumption has been shown to be valid for radars with wavelengths near 10 cm (Greene, 1964).

2) The spatial volume illuminated by the radar beam is completely filled by the target. This condition is not always met, particularly on the periphery of a storm, with a resulting loss of resolution of fine scale detail in such areas (Greene, 1971). However, this effect does not significantly affect the major features in the digital data.

3) The Rayleigh approximation is used to describe the scattering properties of spherical liquid water drops having diameters on the order of 0.04λ , where λ is the radar wavelength in cm. In severe storms, the large, non-spherical water drops and hailstones which may be present do not meet the Rayleigh criteria. However, the enhanced reflectivity of these particles may be useful in identifying such storms.

4) Each digital datum value represents a point in the center of the radar volume.

5) The equivalent radar reflectivity values, Z_e , obtained from the digital data, are representative of a continuous scalar field.

2. Earth Curvature Correction

Microwave radiation propagating in free space will follow a

straightline path. However, the microwave radiation of a radar beam in the atmosphere does not follow a straightline path but instead follows a curved path due to refraction. The amount of curvature of the path depends on the index of refraction (n). Under normal atmospheric conditions where temperature and humidity decrease with height the path of the radar beam curves slightly downward toward the surface of the earth.

Ray theory may be applied to the problem if the change with height of the index of refraction, $\frac{dn}{dh}$, is small. For that case, the exact differential equation for a ray in a spherically stratified atmosphere is

$$\frac{d^2h}{ds^2} = \left(\frac{2}{R+h} + \frac{1}{n} \frac{dn}{dh} \right) \left(\frac{dh}{ds} \right)^2 + \left(\frac{R+h}{R} \right)^2 \left(\frac{1}{R+h} + \frac{1}{n} \frac{dn}{dh} \right) \quad (10)$$

where h is the height of the beam above the earth's surface at a distance s from the transmitter, R is the earth's radius, and n is the index of refraction. Since ϵ , the angle at which the beam is sent out measured from a horizontal plane, is usually very small,

$\left(\frac{dh}{ds} \right)^2 = \tan^2 \epsilon \ll 1$. Also, since $n \approx 1$ and $h \ll R$, Eq. (10) can be reduced to

$$\frac{d^2h}{ds^2} = \frac{1}{R} + \frac{dn}{dh} \quad (11)$$

In this investigation it is necessary to consider the radar beam axis

as a straight line so that a fictitious earth radius given by

$$R' = \frac{R}{1 + \frac{dn}{dh}} \quad (12)$$

must be assumed (Battan, 1973). Since $\frac{dn}{dh}$ is small and nearly linear with a value of $-4 \times 10^{-8} \text{ m}^{-1}$, an earth curvature correction of $R' = \frac{4}{3} R$ is used and the resultant radar beam axis may be considered to be a straight line.

3. The TAMU Weather Radar System

The TAMU Weather Radar System consists of both a 3-cm and a 10-cm radar operating in parallel. Each of the two radar systems has a nearly identical makeup and consists of the following major sub-systems: antenna, conventional analog weather radar set, digital video integrator and processor (DVIP) with plan position indicator (PPI) display, and a nine-track tape unit to record the buffered digital output of the DVIP. Since only 10-cm radar data are used in this study, the following discussion is limited to some of the characteristics of the 10-cm radar.

The 10-cm radar was constructed at TAMU using components from several different radars. The radar receiver is mounted in a CPS-9 console and uses the same synchronizing pulse generator used to trigger the 3-cm radar. This, combined with the common mounting of the 3- and 10-cm antennas, permits simultaneous scanning of the

same illuminated volume by both radars.

The DVIP is a high speed data acquisition, digitizing, and processing system which continuously averages radar logarithmic video output in range (range averaging) and in direction of antenna scan (time averaging) using exponentially weighted digital integrator techniques and synchronized by the radar system trigger. The DVIP installation provides for real-time contoured PPI displays and digital recording of the digital, integrated data.

The DVIP output signal is split into two channels, the digital channel and the display channel. The display channel provides either log video or contoured log video to the PPI scope. The digital output consists of the 1- or 2-km range increment integrated video samples, provided in a buffered 8-bit parallel binary configuration. Each digital output word represents a digital value of the integrated video intensity on a linear scale over the input dynamic range of 80 dB. At the digital output there are 215 2-km or 430 1-km digital samples representing the range increments from 21 through 450 km of range, depending on the range increment selected.

The digital output channel of the DVIP is fed into a 9-track magnetic tape recording unit. This tape drive unit records the digital data in a format that makes it readily accessible by computer and controls the azimuth increment integration of the data.

4. Data Reduction and Display

The digital output of the DVIP is recorded on 9-track magnetic tape which becomes the input to the TAMU Amdahl 470 V/6 computer. Computer processing of the digital radar data is performed using a program developed by Sieland (1977) and modified by McAnelly (1979).

The computer program begins by transforming the spherical coordinate system (r, α, ϵ) of the recorded digital radar data into a cylindrical coordinate system (r, α, h) with three separate height divisions, or partial vertically summed reflectivity (PVSZ) layers. The data are then transformed into a two-dimensional rectangular coordinate system (x, y) and five maps are produced, a zero level (zero-tilt) reflectivity map, the three PVSZ maps, and a map of vertically-integrated liquid water content (VIL). The conversion of coordinate systems requires the use of two interpolation schemes, a Lagrangian linear or cubic interpolation scheme along each radial of data and a quadratic scheme for the conversion to rectangular coordinates. An extensive explanation of these interpolation schemes is contained in Sieland (1977).

The three PVSZ maps are produced by summing the reflectivity values in a vertical column above a given (x, y) point at the surface into the lower layer (0-deg to 15 kft), the middle layer (15 to 35

kft), and the upper layer (35 to 50 kft). The summed values of reflectivity in each layer at each (x, y) point are divided by the number of tilt angles used to produce the sum so that a mean value of the reflectivity is produced. VIL is produced using an algorithm developed by Greene (1971) and is based on the relationship

$$M^* = 3.44 \times 10^{-6} \int_{h_{\text{bottom}}}^{h_{\text{top}}} Z_e^{4/7} dh \quad (13)$$

where M^* is the VIL in units of kg m^{-2} and h is the height in meters.

Because of the large amount of data processed and to reduce computation time, the Sieland program maps only a selected portion of a grid centered on TAMU. The mapped portion is selected by specifying a distance east (-) or west (+) from TAMU to the lower left corner of the 100 x 100 km grid, a distance north (-) or south (+) from TAMU to the lower left corner of the 100 x 100 km grid, a starting azimuth for data processing, and a last azimuth. Computer processing of the data on the 100 x 100 km grid results in a data output spatial resolution of 2-km on a 51 x 51 output array.

The radar data used in this investigation were produced and recorded by the TAMU Weather Radar System during the evening of 2 May 1978 (3 May 1978 GMT), as an area of light and moderate thunderstorm activity moved through the College Station area. Tilt-sequence data were recorded at times which would permit comparison

with GOES satellite data collected that evening at 15-min intervals. This investigation used two tilt-sequences of the radar data for comparison with GOES imagery, the first tilt-sequence beginning at 0022 GMT and the tenth tilt-sequence beginning at 0215 GMT. These tilt-sequences were processed by Mr. Ray McNelly to produce maps of zero-tilt reflectivity, PVSZ in three layers, and VIL.

The maps of zero-tilt reflectivity, PVSZ, and VIL were adjusted for ground clutter effects by excluding all data within a 40 km radius of TAMU in order to avoid data contamination and to assure comparability between results for the zero-tilt reflectivity maps and the PVSZ and VIL maps. Data at the outer edges of the radar maps and along bounding azimuths used by the Sieland program also were excluded due to suspected boundary interpolation problems in the computer program. After these adjustments, the data were tabulated for comparison with the infrared satellite data.

CHAPTER III

GEOSTATIONARY METEOROLOGICAL SATELLITE DATA

Meteorological satellites have been used by meteorologists for both qualitative and quantitative investigations of atmospheric phenomena. Geostationary satellites, by virtue of near-continuous coverage of large areas of the earth surface, permit more detailed examination of severe weather development than is possible through the use of polar-orbiting satellites. The on-board digitization of the data from the newer geostationary satellites makes possible ready comparison of these data with other digital data fields and is useful in the analysis of severe weather occurrences.

1. The SMS/GOES Spacecraft

The Synchronous Meteorological Satellite/Geostationary Operational Environmental Satellite (SMS/GOES) spacecraft is a cylindrical spacecraft weighing approximately 578 kg at launch. The spacecraft are placed into a circular orbit at about 35,800 km above the earth surface. The satellites orbit the earth at a speed c about $11,000 \text{ km hr}^{-1}$. This combination of altitude and speed permits each satellite to remain continuously above the same point on the earth and produces what is referred to as a geostationary or

geosynchronous orbit.

The spacecraft is controlled for proper earth-imaging by an attitude control subsystem which maintains the spin rate at 100 rpm and aligns the spacecraft spin axis parallel to the earth's polar axis. On-board altitude sensors are used to determine the spin axis orientation and a hydrazine jet system is used to adjust the spin axis orientation, spin rate, and orbital position as necessary (Corbell *et al.*, 1976).

The primary purpose of the spacecraft is to provide earth-imaging in the visible spectrum (0.55 to 0.7 μ m) with an 0.9-km resolution at subpoint and in the infrared spectrum (10.5 to 12.6 μ m) with an 8-km resolution at subpoint. The spacecraft also possesses a capability to provide direct, quantitative measurements of solar activity and to collect and distribute environmental data measured on remotely located data collection platforms on the earth's surface and in its atmosphere.

Primary sub-systems aboard the spacecraft include the Visible and Infrared Spin Scan Radiometer (VISSR), the Space Environmental Monitor (SEM), the Telemetry, Tracking, and Command (TTC) sub-system, and an attitude-control sub-system. The VISSR provides earth-imaging in the visible and infrared spectrums. The SEM includes a magnetometer, a solar x-ray telescope, and an energetic

particle monitor. The TTC includes equipment for S-band transmission and reception (in reduced bandwidth) of VISSR data, S-band transmission of weather facsimile data, UHF reception of data from remote data collection platforms and downlink of these data to earth, and VHF and S-band communications equipment for commanding the spacecraft, for telemetry, and for transmitting SEM data. The primary instrument providing the data used by most meteorologists is the VISSR (Corbell et al., 1976).

2. The Visible and Infrared Spin Scan Radiometer

The Visible and Infrared Spin Scan Radiometer scans from west to east in eight identical visible channels and two infrared channels. The sensor provides visible data at 0.9-km resolution at satellite subpoint and infrared data of 8-km resolution at satellite subpoint. The resolution in both the visible and infrared data deteriorates for points away from the satellite subpoint. With the satellite rotating at 100 rpm, the VISSR scans the earth for about one-twentieth of each complete rotation. The radiometer performs 1821 steps in successive scans from north to south in 18.2 min and provides an image of the complete earth disc or about one quarter of the earth's surface. The resulting visible images contain 14,568 lines. The infrared images have a total of 1821 lines. In addition to the normal scanning

mode, the spacecraft may be placed into a limited scan mode. In the limited scan mode the north-south scan may be limited to a fewer number of scan lines, thereby reducing the area of coverage but increasing the frequency of imaging.

The VISSR senses radiation in both the visible and infrared spectrums. Radiation is received by the VISSR's primary optics via a 45° object-space scan mirror. The mirror is an elliptically shaped plane mirror which is tilted about its minor axis to obtain the north-south scan steps. West-east scans are produced by spacecraft rotation about the spin axis. Energy from the scan mirror is collected by a Ritchey-Chretien optical system which includes a baffle that extends from the mirror to minimize the effects of scattered radiation. Radiation in the visible spectrum is detected at the prime focus using eight fiber optics in a linear array at the focal plane. The other ends of the fibers are optically integrated with eight photomultiplier tubes having the desired 0.55- to 0.70- μm response. The prime focal plane is also relayed to the long-wavelength HgCd/Te detector using two germanium relay lenses. An optical filter between the final relay lens and the detector restricts the radiation to the 10.5- to 12.6- μm wavelength band (McKowan, 1977).

3. Data Distribution and Processing

The SMS/GOES VISSR data are distributed as indicated in Fig.

1. Raw data are read out and preprocessed at the Command and Data Acquisition (CDA) station at Wallops Island, Virginia. The CDA processes the data to reduce the data rate by about 16 to 1 for simplification of data transmission and then transmits these stretched data back to the satellite. Lower resolution infrared data are formatted for analog transmission and are sent via telephone lines from the CDA to the Satellite Field Service Stations (SFSS) and to the Central Data Distribution Facility (CDDF) at Marlow Heights, Maryland.

The stretched data are retransmitted by the satellite to the National Environmental Satellite Service (NESS) facility at Suitland, Maryland, and to other facilities with a direct readout capability. The NESS-Suitland complex relays the stretched data via microwave link to the CDDF. The CDDF formats the data and prepares it for transmission to SFSS's throughout the country. Enhancement of the infrared data to emphasize specific features in the imagery can be accomplished both by the CDA at Wallops Island and by the CDDF.

GOES/SMS VISSR data are available to many users through a "GOES-Tap" program using high-quality telephone line transmission of the data from an SFSS to the user. As an alternative, some facilities have developed a direct readout capability for receiving the stretched VISSR data (Corbell et al., 1976).

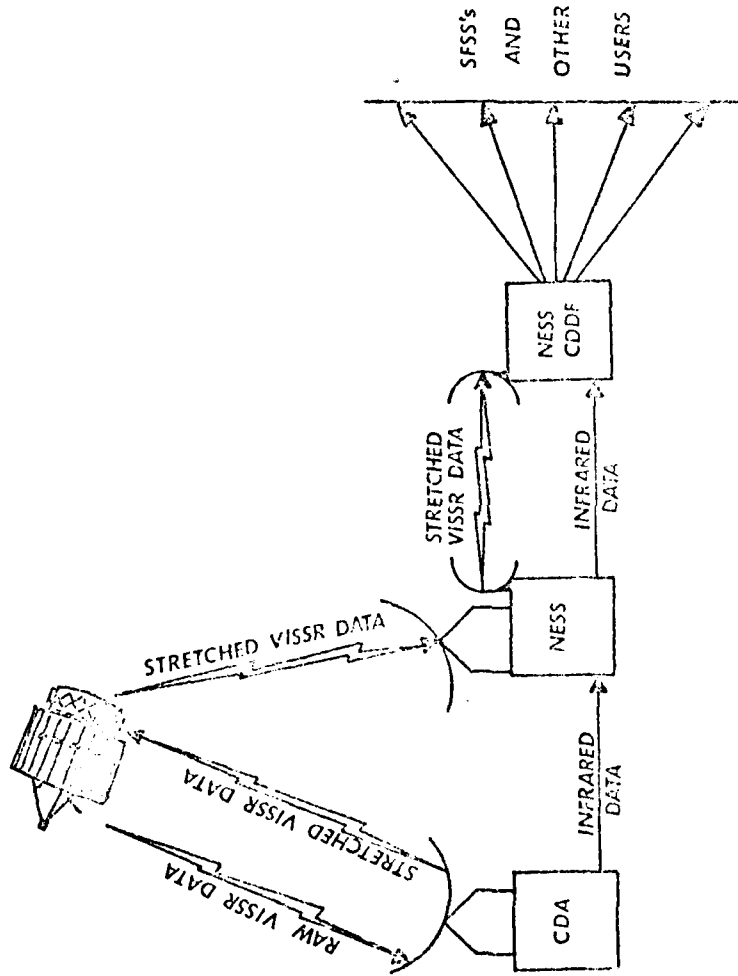


Fig. 1. SMS/GOES Data Distribution.

4. Basic Characteristics of Infrared Satellite Data

Infrared radiation is emitted by objects at an intensity that depends on the temperature of the body. If the object is assumed to emit radiation as a "black body," i.e., to absorb all radiation falling upon it without reflecting any of the incident radiation, then the monochromatic intensity of the emitted black body radiation is given by Planck's Law,

$$E = 3.74 \times 10^{-5} \lambda^{-5} \left(\exp \frac{1.4385}{T} - 1 \right)^{-1} \quad (1)$$

where λ (cm) is the wavelength of the emitted radiation and T (K) is the temperature of the black body (Haltiner and Martin, 1957). The proportionality between the temperature of the target and the intensity of the infrared radiation emitted by the target forms the basis for all infrared imaging.

Infrared sensors aboard meteorological satellites measure long-wave (usually 10.5- to 12.6- μ m wavelength) radiation emitted by cloud, land, and water surfaces. These measurements may be converted to black body temperatures which generally represent the temperatures of the surfaces viewed. This characteristic of infrared satellite imagery is especially useful in that it permits an approximate evaluation of the height of various clouds when the atmospheric temperature is known from upper-air data. The association of cold

cloud tops apparent in infrared data, convective activity, and precipitation suggested by some of the authors cited in Chapter I forms the basis for much of the following material in this investigation.

5. McIDAS Data

The Man-computer Interactive Data Access System (McIDAS) was developed by the Space Science and Engineering Center (SSEC) at the University of Wisconsin as a means of obtaining easy access to satellite data in the time domain for examining atmospheric weather systems as dynamic systems (Smith, 1975). The operator using McIDAS views image and graphics data on a large color television monitor. Images may be viewed in single frames or sequences and may be enhanced, colorized, or combined at the choice of the operator. Control of the system is effected from the operator's console by means of twin joysticks and a keyboard. The operator also may be supported by hard copy generating devices such as line printers and graphics plotters (Haig, 1978).

Image data used by the McIDAS also may be saved on magnetic tape for later use or for the use of other investigators. The imagery used in this study was produced in such a fashion by the McIDAS at the SSEC in Madison, Wisconsin.

McIDAS image save tapes contain two-dimensional image sectors prepared from a variety of image sources. The data for this study

are a sequence of infrared images from the GOES-East satellite taken between 0015 GMT and 0345 GMT on 3 May 1978. The data are stored on the tapes in a directory record which contains date, time, and line and element coordinate information necessary for image processing and in image sector records which follow the directory record. Each image sector record contains six lines of GOES data in 24-bit words so that for a complete image of 500 lines a total of 84 image sector records is required. The directory record is 225 words long and each image save record is 2241 words long (6723 8-bit bytes). 6720 bytes of each image save record are used for data with the remaining 3 bytes containing a record sequence counter (Young, 1978).

Full-resolution GOES-East infrared imagery are used in this study. Each pixel, or picture element, has a resolution of approximately 8 km in the line direction (N-S at satellite subpoint) and 4 km in the element direction (E-W at satellite subpoint). The McIDAS artificially subdivides each pixel to a 4 km by 4 km pixel on the image save tapes. Line and element numbering in the infrared data is based on the system used for full-resolution visible data (Young, 1978).

6. Data Reduction and Display

Use of the McIDAS image save tapes required development of procedures to navigate, or locate, the image pixels, to map the infrared data into the grid used for the digital radar data, and to correct the data for displacement error due to cloud height.

a. Image Navigation

Navigating the image pixels requires extensive computer software that was not available for this investigation. Instead, Mr. J. T. Young of the SSEC provided line and element navigation solutions for four latitude and longitude points in a grid around TAMU for each hour from 0000 GMT to 0400 GMT on 3 May 1978. A fourth-order polynomial was then fitted to the line and element solutions for each point to permit interpolating line and element solutions for intermediate times. The interpolated line and element solutions then were used as inputs to a computer program called MACMAP 3 which produced mapping equations to map the satellite data into the radar grid.

b. Mapping the Satellite Data to the Radar Grid

The satellite data array is a two-dimensional array arranged by line and element number. The radar grid centered on TAMU can be regarded as an (x, y) array with a positive y -axis oriented due North and a positive x -axis oriented due East. The variation in

line and element solutions for the four points navigated by the SSEC suggested that simple bi-linear relationships of the form

$$\text{line number} = a x + b y + c \quad (2)$$

$$\text{element number} = d x + e y + f \quad (3)$$

could be used to relate the digital satellite line and element numbers to the coordinates of the radar grid, where the constants a , b , c , d , e , and f are determined by solving three simultaneous equations using solutions for three of the four points navigated by the SSEC. The original mapping program, MACMAP 1, used navigation solutions for three points to produce coefficients for the mapping equations and used the remaining solution for the fourth point to check the accuracy of the equation. MACMAP 1 solutions produced results accurate to one half pixel for the fourth point for all images except two and was within one pixel for those two images.

An effort to produce more accurate mapping of the satellite data resulted in adding new terms to the mapping equations using the fourth point to determine "correction factors" k_1 and k_2 . The new equations were of the form

$$\text{line number} = a x + b y + c + k_1(x-x_0)(y-y_0) \quad (4)$$

$$\text{element number} = d x + e y + f + k_2(x-x_0)(y-y_0) \quad (5)$$

where the coefficients a , b , c , d , e , and f are determined by solving simultaneous equations for the three original points and the correction

factors by determining the difference between the SSEC navigation solutions and the solutions from Eq. (2) and Eq. (3). The values of the constants x_0 and y_0 are determined from the "common values" of x and y shared by the three points used to solve the simple bilinear equations. Fig. 2 illustrates the general arrangement of the four navigated points relative to TAMU and the radar grid and illustrates how x_0 and y_0 were determined.

The *M/C*MAP 3 computer program produced coefficients for Eq. (4) and Eq. (5) for each of the images used in this study. The solutions produced accurate results for all four points originally navigated by the SSEC and accurate line number solutions for TAMU coordinates in a later check. A check of the element coordinate for TAMU was not accurate in the later check due to loss of the original input "gamma shifts" used to produce the SSEC solutions.

The procedure adopted in the remainder of this study depended upon the following assumptions:

- 1) The navigation solutions produced for the four points by the SSEC are accurate. Young (1978) suggests an accuracy to within one line number and within two element numbers in the full-resolution visible data. The numbering system for lines and elements in the infrared data is based on that for the visible data and is incremented by a factor of four which suggests an accuracy to the nearest pixel

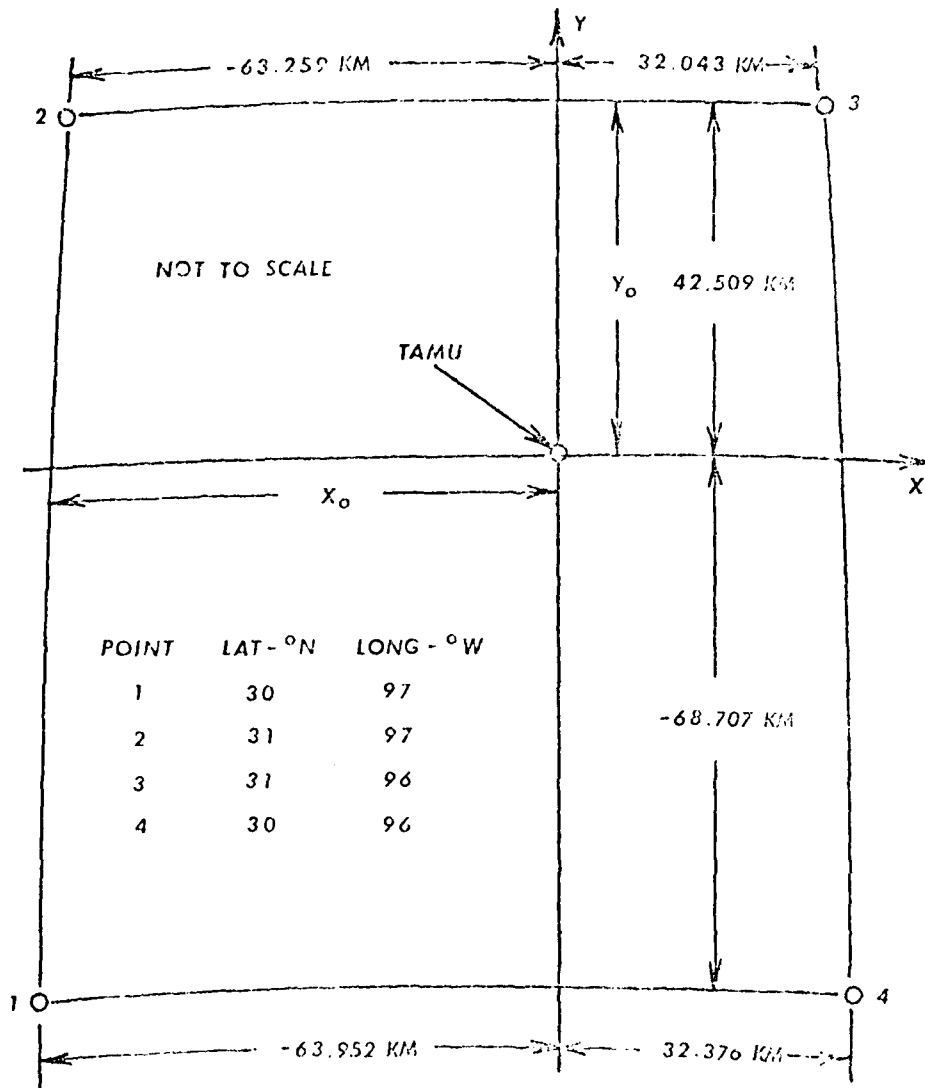


Fig. 2. Navigated points and mapping to the digital radar grid.

in the infrared data.

2) Interpolation in time using a fourth-order polynomial produces accurate solutions for intermediate image times. This assumption is required as a compromise to avoid the computer costs associated with providing SSEC solutions for images at 15-min intervals over 4 h and for four points in each image. The variation with time of the original SSEC solutions suggests that this assumption is valid.

3) Mapping equations of the form of Eq. (4) and Eq. (5) provide an accurate coordinate transformation between the line and element coordinates of the satellite image array and the (x, y) coordinates of the digital radar grid. MACMAP 3 mapping solutions provided accurate results for the SSEC solutions for all four navigated points and for TAMU coordinates. Comparisons of contoured fields of infrared data mapped using MACMAP 3 solutions to hard copy enhanced GOES infrared imagery also confirm the general accuracy of the mapping procedure. It is evident, however, that the earth curvature considerations used in establishing the radar grid for MACMAP 3 would not compensate for such effects at distances far removed from the center of the grid. For studies of data within 200 km of TAMU the MACMAP 3 procedure appears to yield satisfactory results.

Actual production of maps of satellite data depended upon development of programs designed to use MACMAP 3 solutions for the coefficients of Eq. (4) and Eq. (5). The original program was called MACVIS and was designed to map full-resolution visible GOES data to the radar grid. Problems with brightness normalization due to a very large solar zenith angle led to abandoning the use of the visible data after MACVIS was developed. The MACIR computer program was developed from the MACVIS program and is designed to use solutions to Eq. (4) and Eq. (5) to map GOES infrared satellite data into the radar grid centered on TAMU.

MACIR is a modular computer program using two function sub-programs to produce solutions to Eq. (4) and Eq. (5) and using subroutines to save an array of satellite data that just overlaps the area of the radar grid that is of interest and to map the saved data array into the radar grid. Subroutine BOUND determines bounding line and element numbers so that the saved satellite data can be extracted from the image sector records on the McIDAS image save tapes. Subroutine DATSAV reads the image sector records and saves the GOES data between the bounding line and element numbers determined by BOUND. Subroutine DATMAP computes a line and element number for each (x, y) point in the portion of the radar grid selected for analysis and assigns the value of the pixel corresponding

to that (line, element) pair to the (x, y) point in the radar grid.

The data thus mapped are stored in an array called IGOES. Subroutine OUTPUT1 is used to print maps of the IGOES array and is readily adapted to varying grid spacing.

The MACIR program was used to produce maps of the 0015 GMT, 0030 GMT, 0215 GMT, and 0230 GMT GOES-East images for 3 May 1978 for this investigation. Maps of all the images between 0015 GMT and 0345 GMT also were produced for a different study. The maps consisted of point values of GOES-East infrared data printed at 2-km intervals for this investigation and 4-km intervals in the other maps. A listing of the MACMAP 3 and MACIR programs is contained in Appendix A.

c. Correction for Displacement Error Due to Cloud Height

Cloud interpretation near the horizon of a geostationary satellite image is complicated by the effect of curvature of the earth surface. Near the satellite subpoint on the earth's surface, the apparent and actual cloud positions coincide. However, the difference between the apparent and actual positions increases as the cloud's distance from the subpoint increases. In order to locate accurately a cloud feature in a geostationary satellite image it is necessary to compensate for this effect by making a displacement correction toward the satellite subpoint. Weiss (1978) gives a method of correcting

SMS images for this effect and that method was used to compute displacement errors for various cloud heights using a GOES-East subpoint of 0.335° S, 75.021° W. Displacement corrections were computed for TAMU for various cloud heights and are listed in Table 1.

Table 1. Displacement corrections for cloud height.

Cloud Height (km)	Displacement Correction (km)
10	9.17
12	11.00
14	12.83
16	14.66

Cloud height was determined by converting an average digital count for each image to an equivalent black body temperature and selecting the ICAO standard height corresponding to that temperature in the 2350 GMT College Station sounding. For temperatures near and above the tropopause a different procedure was used. The saturation adiabat from the convective condensation level was used to determine an equilibrium level on the sounding. Above this level a subjective estimation of the temperature of convective tops based on approximately 20 per cent mixing with environmental air was

used to determine a temperature-height relationship.

Rather than attempt to shift each point in each satellite image toward the satellite subpoint an amount dependent upon the individual digital count at each point, a uniform shift of the data toward the satellite subpoint based on the average digital count for the image was used. This procedure was adopted to avoid computational problems and to prevent creation of "shadows" in highly contoured infrared data fields. Table 2 lists the magnitudes of the corrections applied to the images in this investigation.

Table 2. Displacement correction for each image.

Image Time	Average Digital Count	x Displacement (km)	y Displacement (km)
0015Z	190	5	8
0030Z	204	6	9
0215Z	211	6	9
0230Z	218	7	11

After the GOES infrared images were mapped to the radar grid and corrected for displacement error due to cloud height, the data for these images were tabulated along with corresponding radar data in the three radar data sets. These data then formed the three data sets examined in this investigation.

CHAPTER IV

COMPARISON OF DIGITAL RADAR AND SATELLITE DATA

Comparison of the fields of digital radar and digital satellite data was performed by first qualitatively comparing contoured maps of the data and then objectively comparing the fields by computing correlation coefficients between the radar and satellite data using the SAS 76 statistical analysis system (Barr et al., 1976) as implemented on the Amdahl 470 V/6 computer at TAMU.

1. The Basis for the Comparison

Meteorological radars examine the structure of weather systems by emitting electromagnetic energy in the microwave portion of the electromagnetic spectrum and measuring the amount of that energy scattered back to the radar by hydrometeors of various sizes and shapes associated with the weather system. Meteorological satellites examine weather systems by sensing the intensity of scattered or emitted electromagnetic energy from the cloud structures and, ultimately, from the hydrometeors that make up the clouds themselves. Sensors aboard meteorological satellites typically respond to electromagnetic radiation in the visible and infrared portions of the electromagnetic spectrum although ultraviolet and

microwave sensors have been used for special applications.

Since both meteorological radars and meteorological satellites examine weather systems by the use of scattered or emitted electromagnetic radiation at different wavelengths, it is reasonable to expect that some relationship should exist between meteorological radar data and meteorological satellite data that are coincident in time and space. The basic purpose of this investigation is to determine if such a relationship exists and, if so, to measure the strength of such a relationship.

To examine the relationship between meteorological radar data and meteorological satellite data, two tilt-sequences of digital radar data and four infrared GOES-East satellite images were examined. The first tilt-sequence was selected early in the data collection period when radar-detected weather activity in the area was relatively weak and just beginning to develop. GOES-East images collected just prior to initiating the tilt-sequence and at its conclusion were used for the comparison. The second tilt-sequence was selected from a later time interval in which line convective activity in the TAMU area had reached near-maximum intensity for the data collection period. Comparison GOES-East infrared images also were selected for times closely corresponding to initiation and termination of the tilt-sequence. The results of the comparisons of

these tilt-sequences with the corresponding satellite data are presented in the following sections.

2. First-Tilt-sequence and Corresponding GOES Images

The first digital radar tilt-sequence was collected from 0022 GMT to 0030 GMT on 3 May 1978. The data were collected in 14 1° inclinations of the radar antenna with each change in antenna angle being made at the conclusion of a 360° sweep. Data from the northwest sector of the tilt-sequence were processed by the Sieland (1977) computer program. The 0015 GMT and 0030 GMT GOES-East infrared images were used for comparison with this tilt-sequence. Maps of zero-tilt reflectivity (dBZ), low-, mid-, and upper-level PVSZ (dBZ), and VIL (kg m^{-2}) are presented in Figs. 3, 4, 5, 6, and 7, respectively. Contoured maps of infrared digital count for the 0015 GMT and 0030 GMT GOES-East images for corresponding areas are presented in Figs. 8 and 9, respectively. Conversion from infrared digital count to equivalent black-body temperature can be approximated by using Fig. 10.

Significant features to note in the digital radar data include a marked absence of indications of echo activity in the upper-level PVSZ map (Fig. 6) and the VIL map (Fig. 7). Echo activity of weak to moderate intensity is indicated in the zero-tilt reflectivity

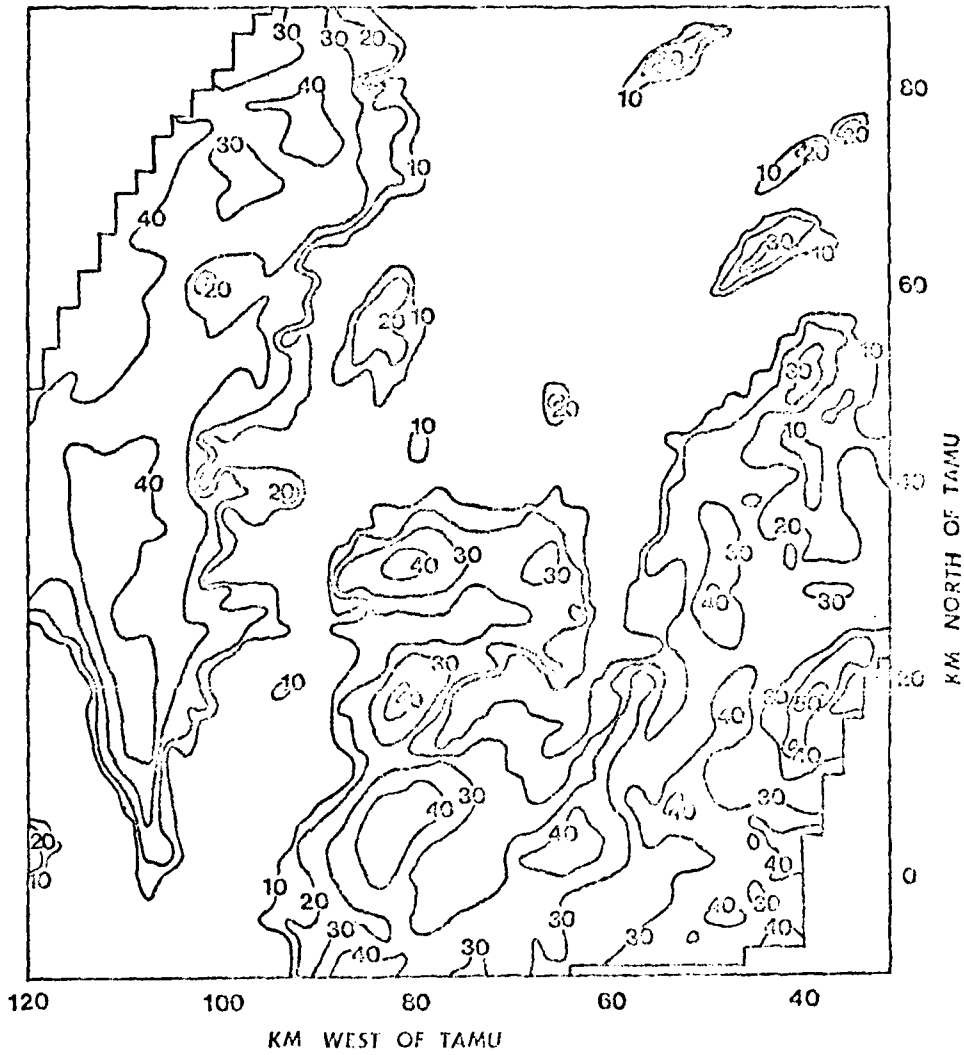


Fig. 3. Tilt-sequence one, zero-tilt reflectivity (dBZ). Data collected on 3 May 1978 at 0022 GMT.

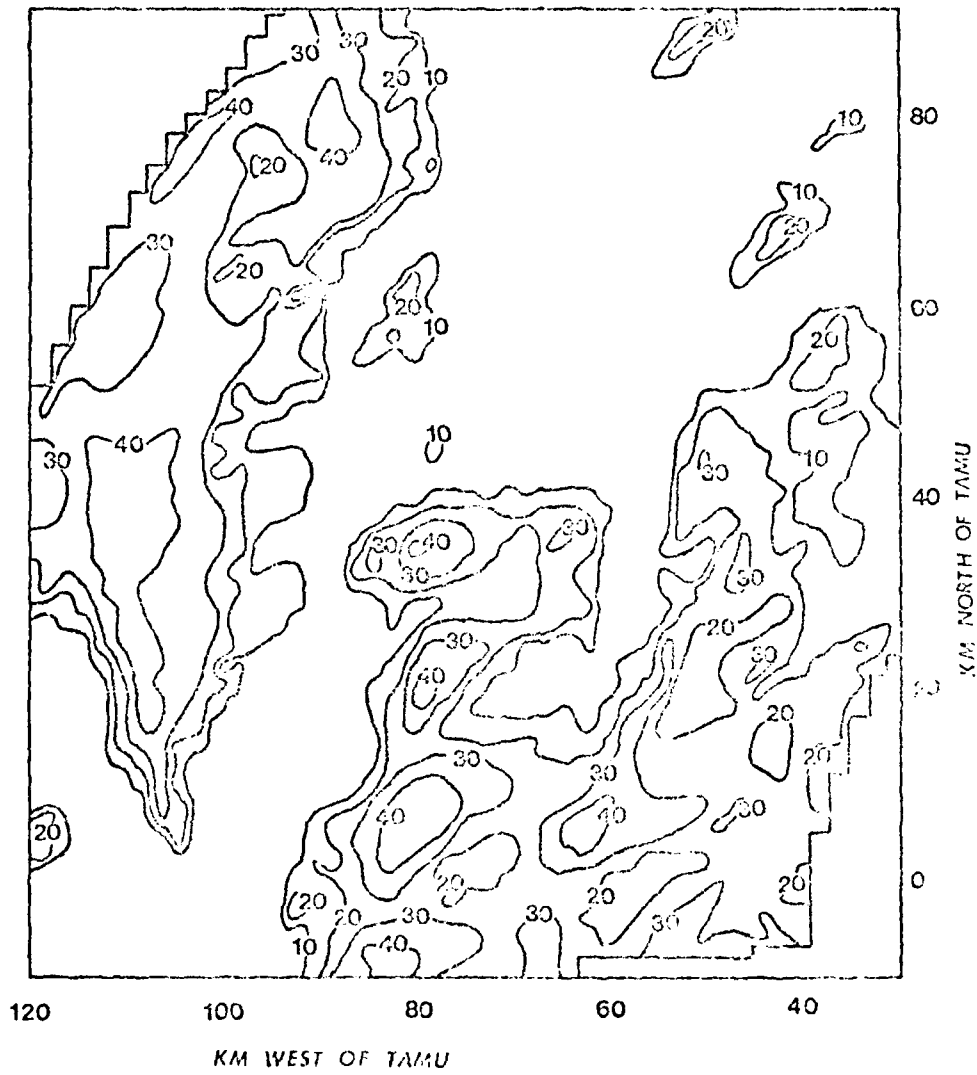


Fig. 4. Tilt-sequence one, low-level PVSI (dBZ). Data collected on 3 May 1978 from 0022 GMT to 0036 GMT.

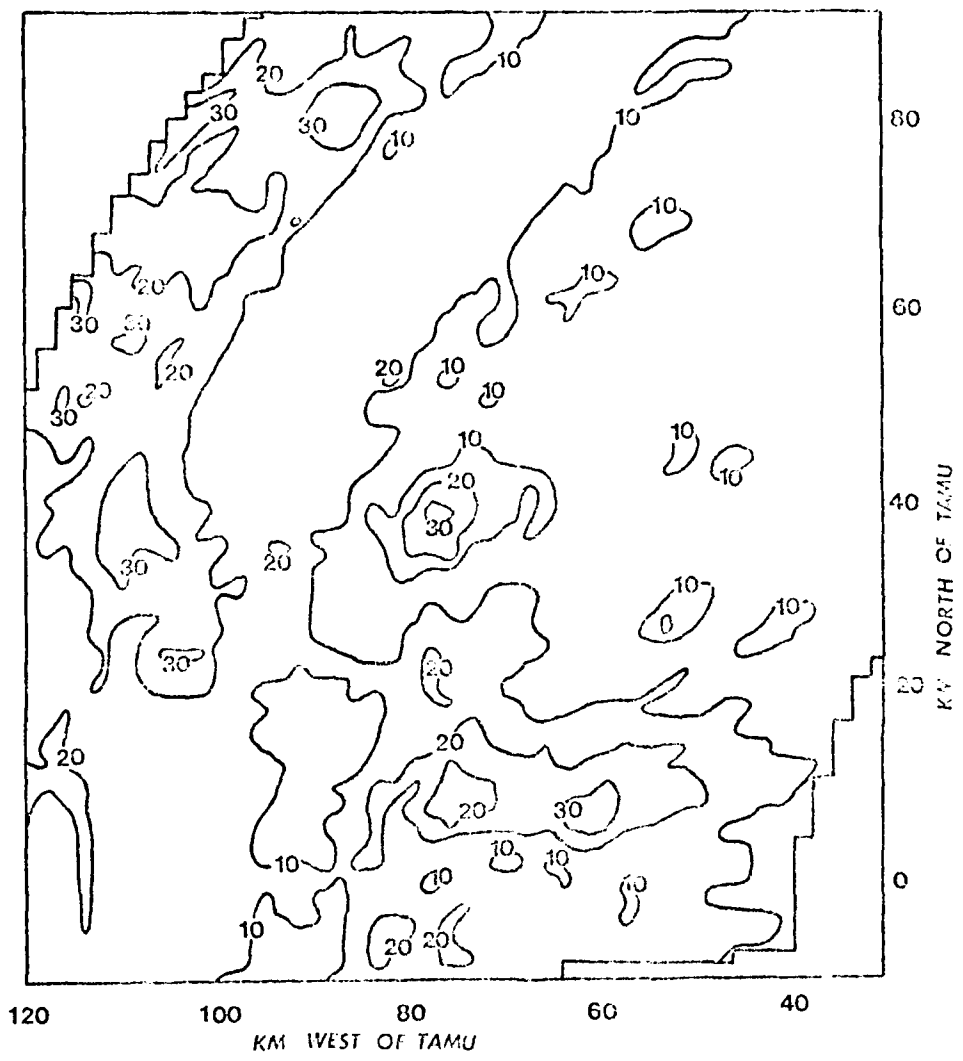


Fig. 5. Tilt-sequence one, mid-level PVSZ (dBZ). Data collected on 3 May 1978 from 0022 GMT to 0030 GMT.

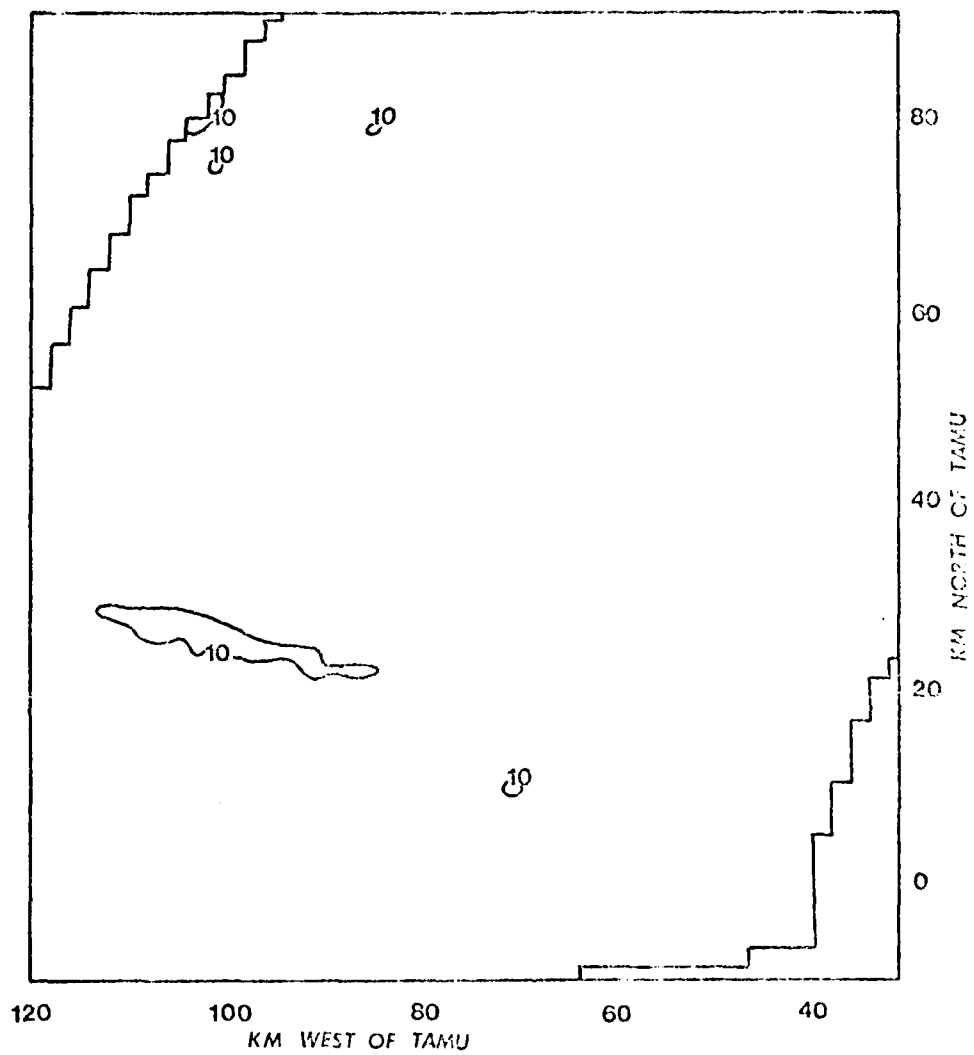


Fig. 6. Tilt-sequence one, upper-level PVSZ (dBZ). Data collected on 3 May 1978 from 0022 GMT to 0030 GMT.

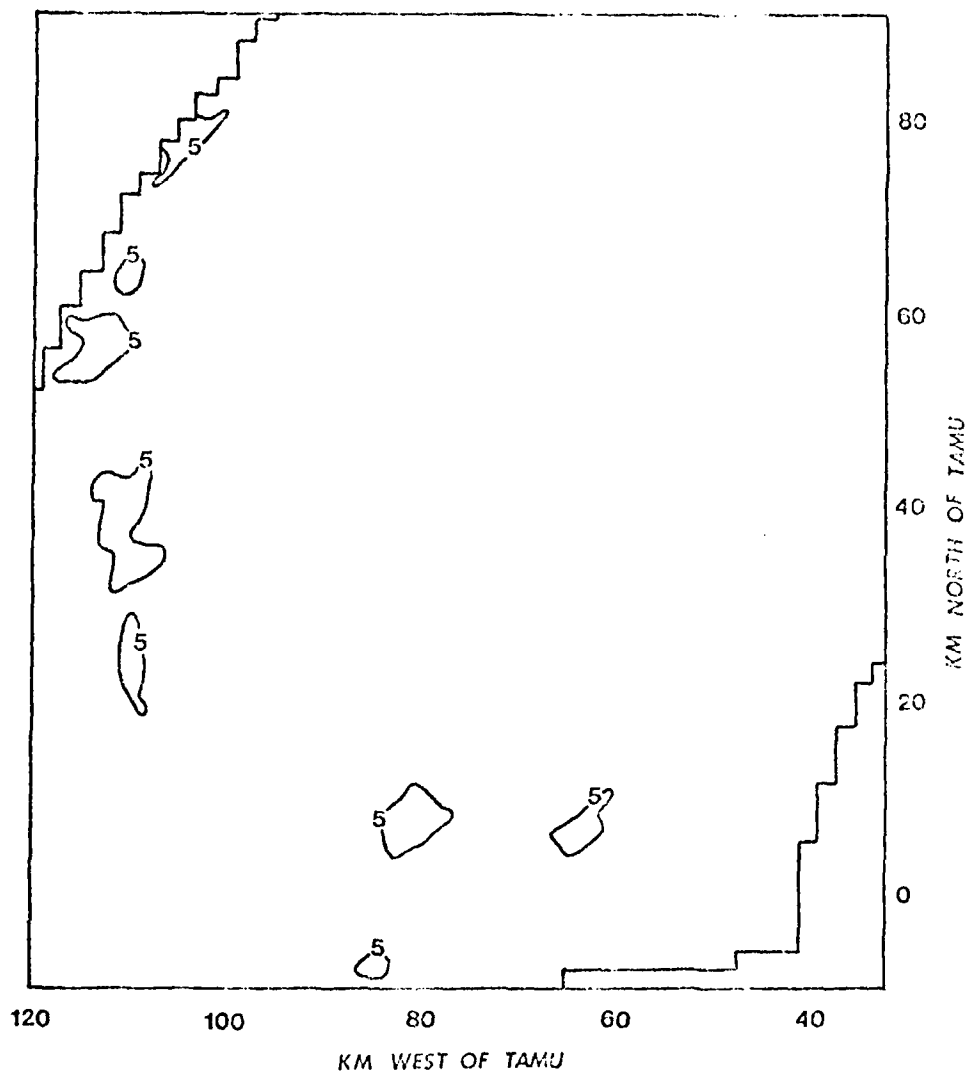


Fig. 7. Tilt-sequence one, VIL (kg m^{-2}). Data collected on 3 May 1978 from 0022 GMT to 0030 GMT.

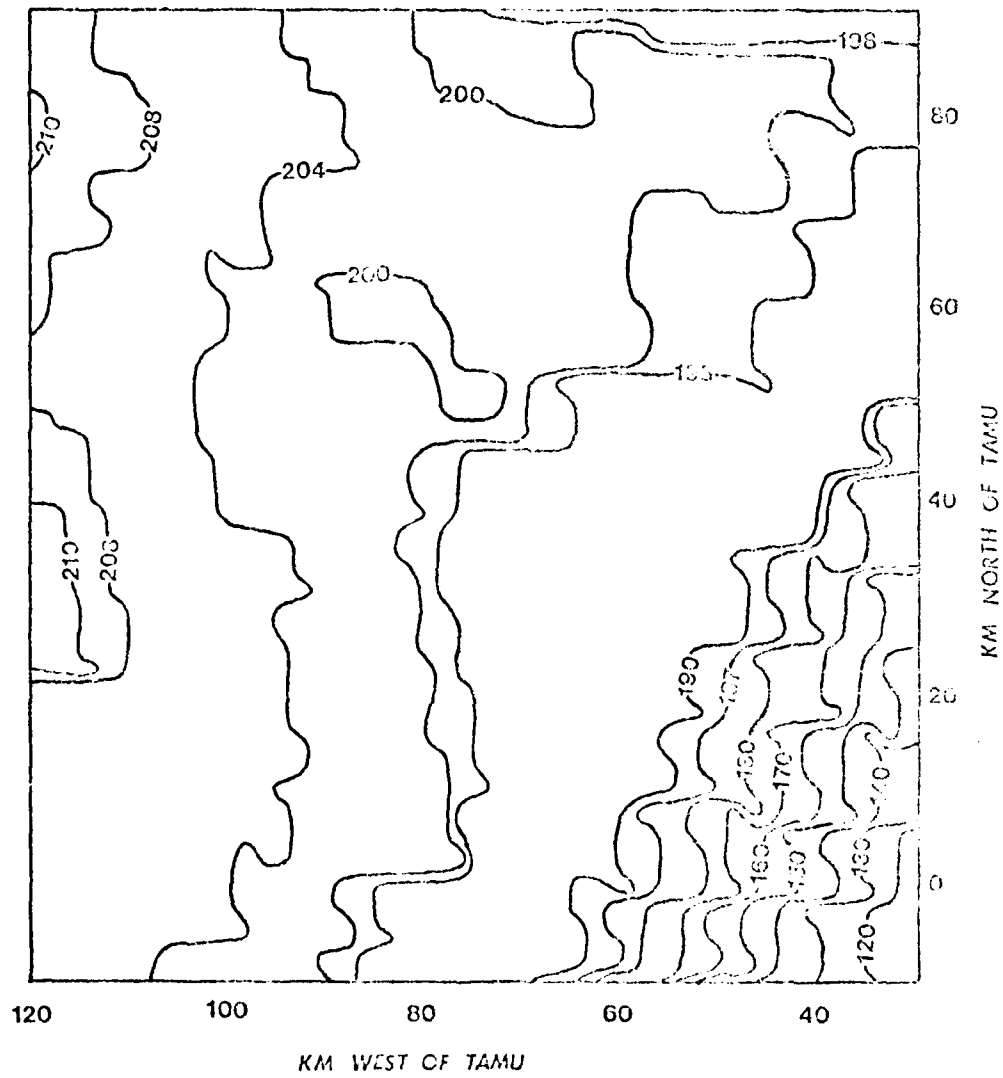


Fig. 8. 0015 GMT, 3 May 1978 infrared image.

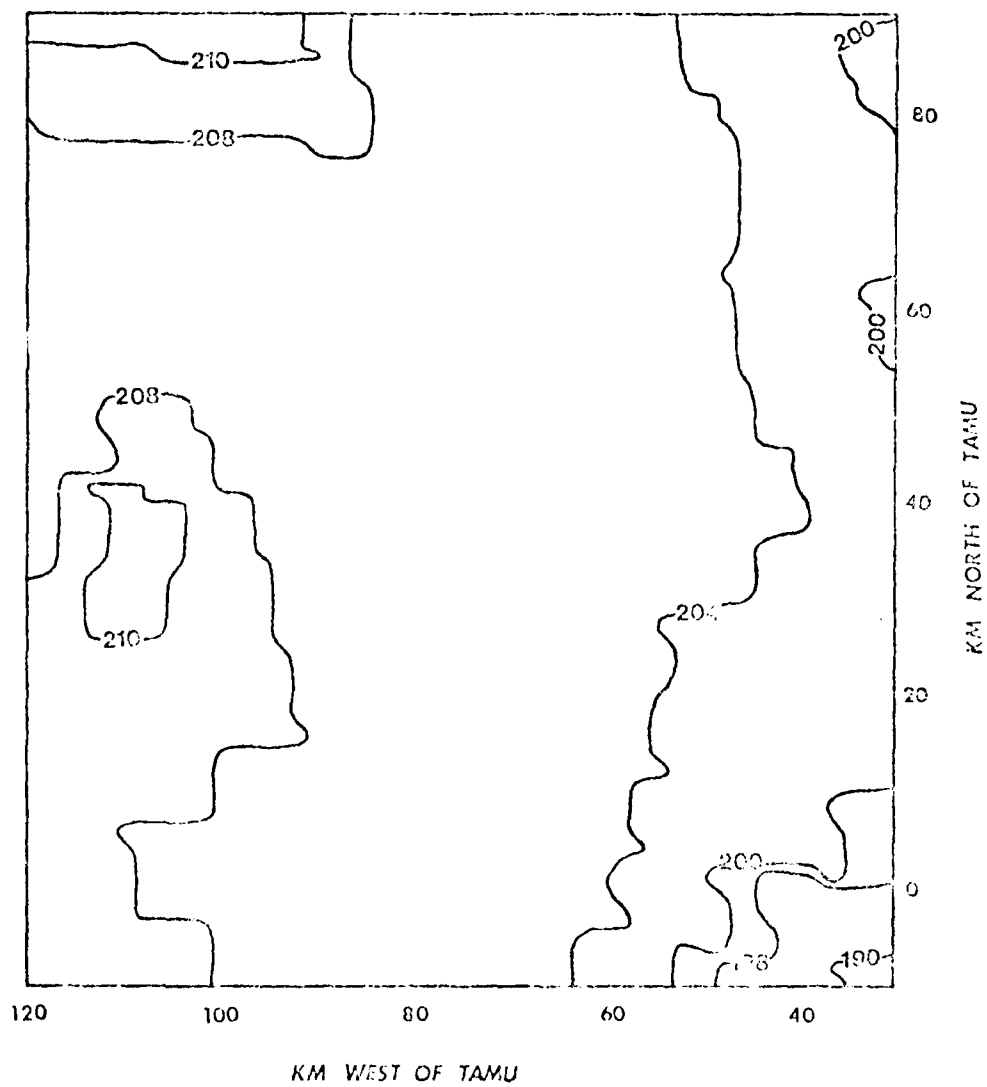


Fig. 9. 0030 GMT, 3 May 1978 infrared image.

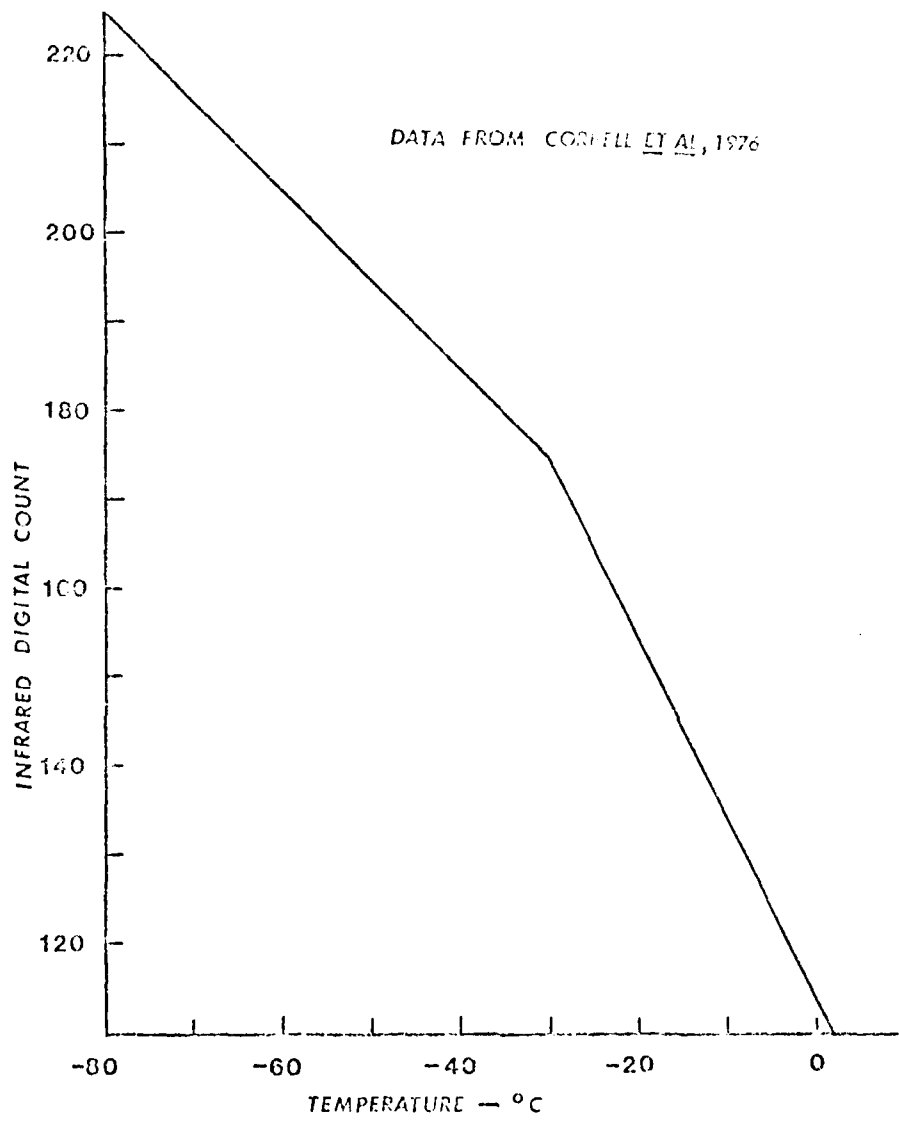


Fig. 10. GOES infrared digital count to temperature calibration.

map (Fig. 3), the low-level PVSZ map (Fig. 4), and in the mid-level PVSZ map (Fig. 5). The best-organized echo activity is located in the western and south-central portions of Figs. 3 and 4.

The 0015Z infrared image (Fig. 8) has a near-uniform gradient of digital count from high values to low from northwest to southeast. The sharp increase in gradient in the southeastern portion of the image is probably caused by the sensor "looking at" lower-level cloud or the side of convective activity. The shapes of the contours for digital counts of 208 and 210 suggest some association with convective activity as evidenced in that area by Figs. 3, 4, and 5.

The 0030Z infrared image (Fig. 9) has a relatively flat gradient of digital count over much of the mapping. The closed 210 contour suggests its relation to convective cells shown in the same area in Figs. 3, 4, and 5. The relative flatness of the gradient of digital counts on the order of 200 and the disappearance of the low values of digital count in the southeast corner of the image suggest the spreading of cirrus cloud cover over much of the area. Obscuration by the cirrus prevents direct observation of low- and mid-level convective activity by the infrared sensor. This effect, when coupled with the coarser resolution of the infrared sensor as compared with the digital radar, is considered to be one of the chief problems in attempting to relate the two types of data.

3. Tenth Tilt-sequence and Corresponding GOES Images

The tenth digital radar tilt-sequence was collected from 0216 GMT to 0233 GMT on 3 May 1978 using 14 1° changes in antenna inclination. Data from the northwest and southwest sectors of the tilt-sequence were processed by the Sioland computer program. The 0215 GMT and 0230 GMT GOES-East infrared images were used for comparison with both sectors from this tilt-sequence. Maps of zero-tilt reflectivity (dBZ), low-, mid-, and high-level PVSZ (dBZ), and VIL (g m^{-2}) are presented in Figs. 11, 12, 13, 14, and 15, respectively, for the southwest sector and in Figs. 18, 19, 20, 21, and 22, respectively, for the northwest sector. Maps of contoured infrared digital count from the 0215 GMT and 0230 GMT GOES-East images for corresponding areas are presented for the southwest sector in Figs. 16 and 17 and for the northwest sector in Figs. 23 and 24.

a. Southwest Sector

Significant features to note in the digital radar data include the presence of strong line radar echoes to the south-southwest of TAMU in all of the digital radar maps. The two areas of heaviest convective activity are especially evident in the mid- and upper-level PVSZ maps (Figs. 13 and 14) and in the VIL map (Fig. 15). The two strong cells exhibit very little "tilt" in the vertical in a comparison of Figs. 12 through 14. Maxima in the VIL map also correspond well

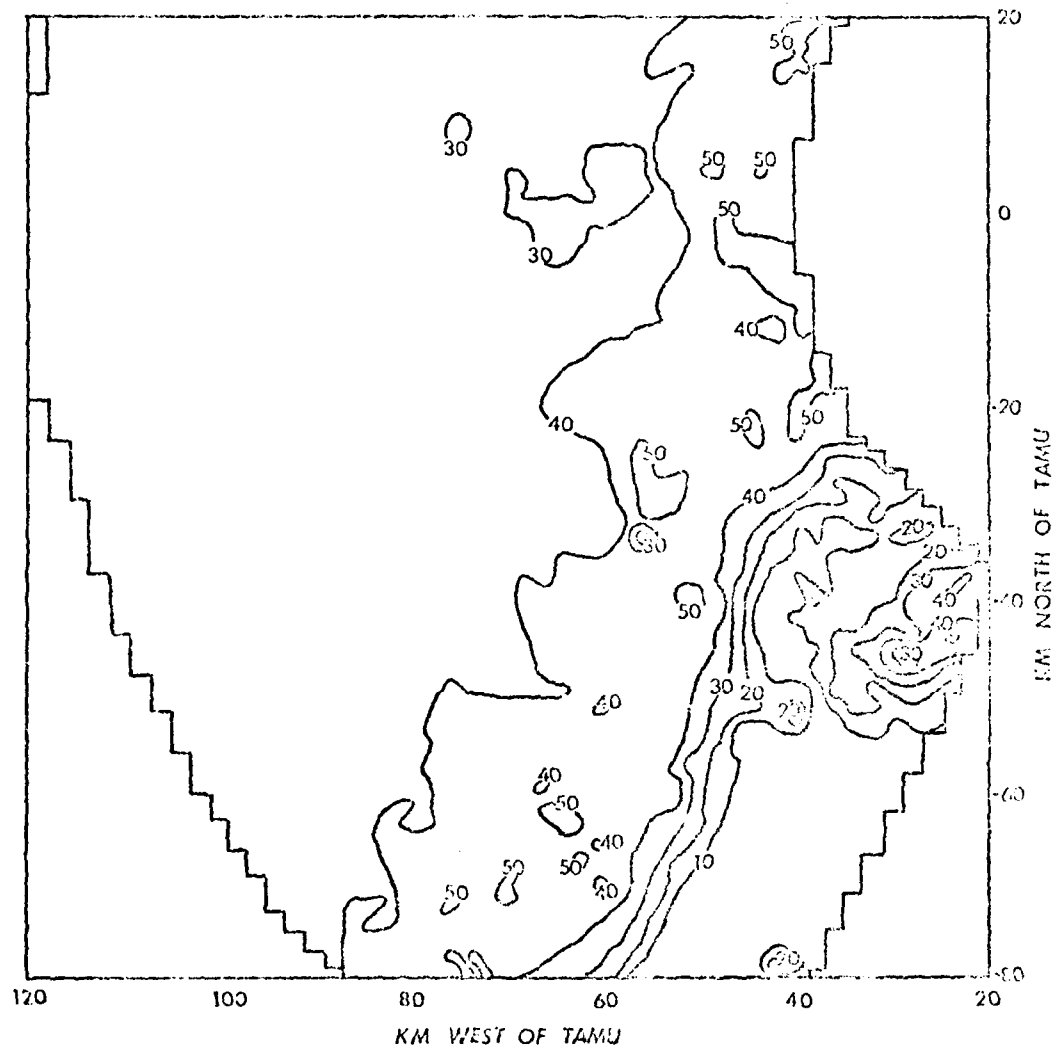


Fig. 11. Tilt-sequence ten, southwest sector, zero-tilt reflectivity (dBZ). Data collected on 3 May 1978 at 0216 GMT.

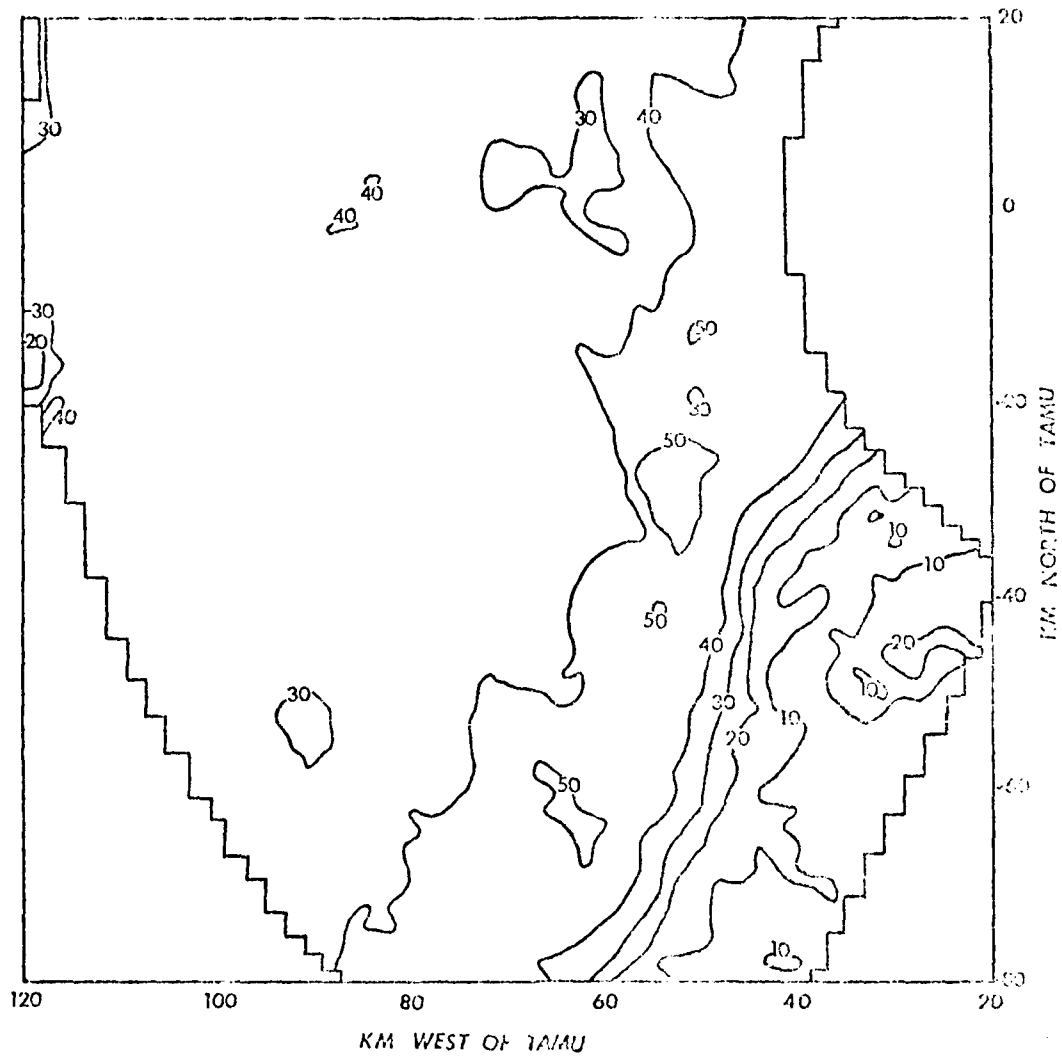


Fig. 12. Tilt-sequence ten, southwest sector, low-level PVSZ (dBZ). Data collected on 3 May 1978 at 0216 GMT to 0233 GMT.

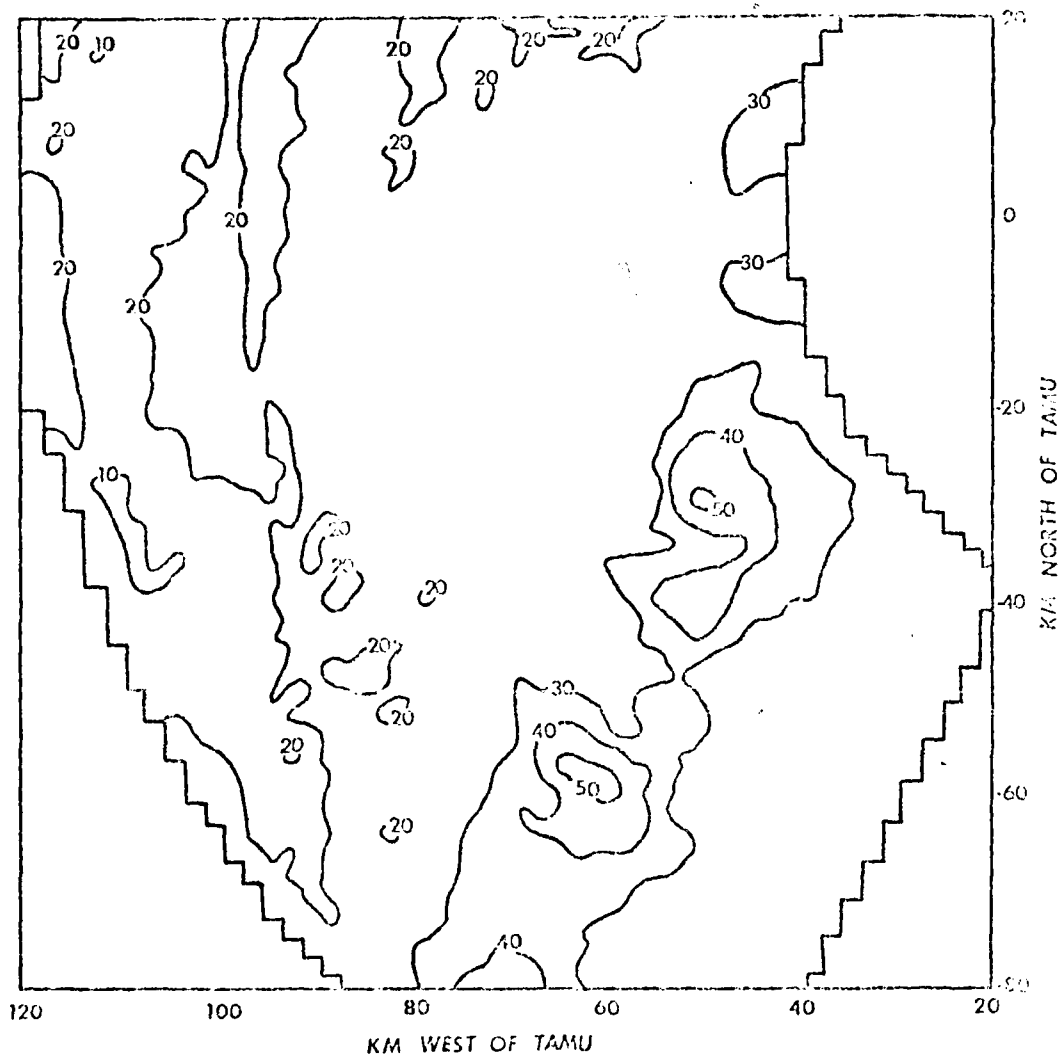


Fig. 13. Tilt-sequence ten, southwest sector, mid-level PVSZ (dBZ). Data collected on 3 May 1978 from 0216 GMT to 0233 GMT.

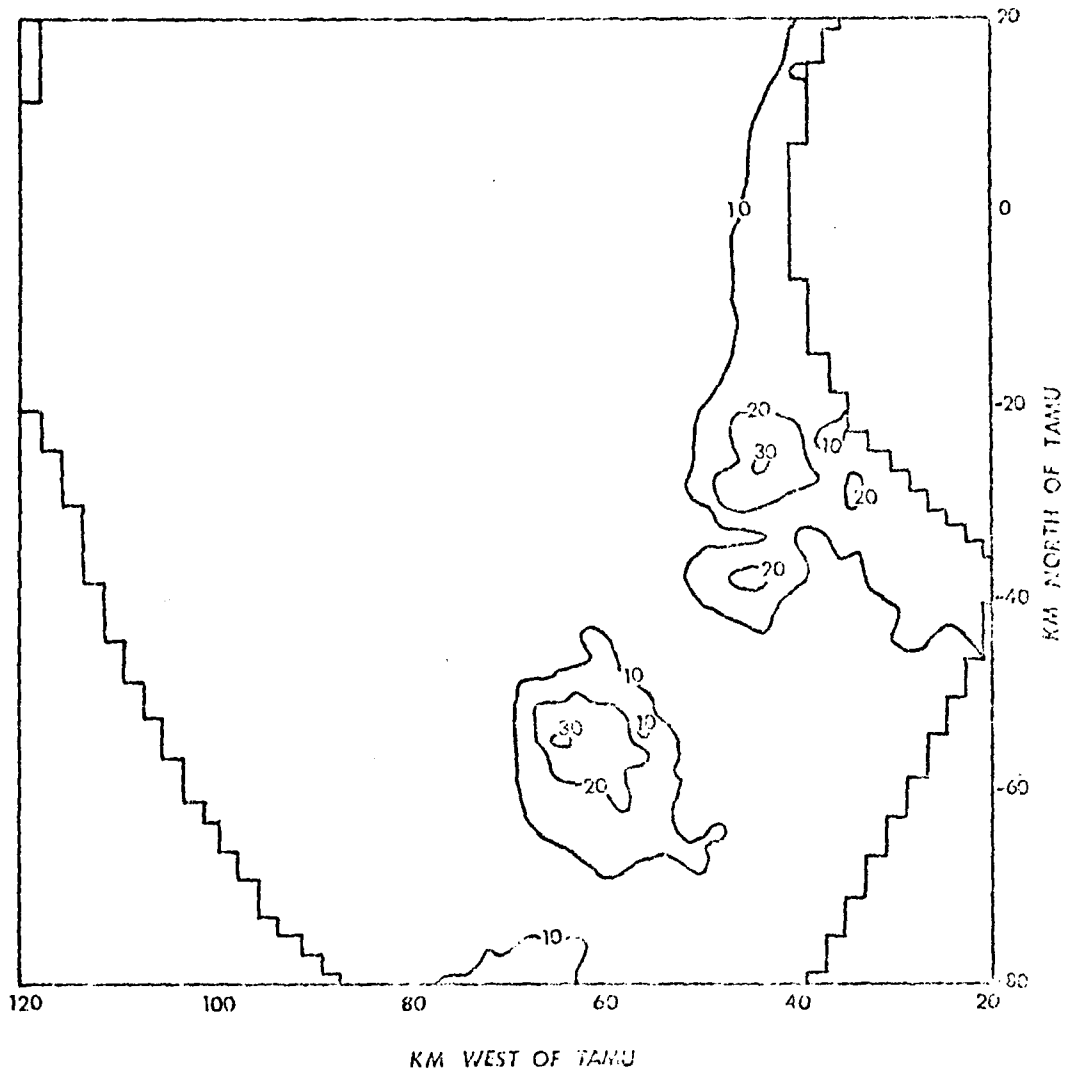


Fig. 14. Tilt-sequence ten, southwest sector, upper-level PVSZ (dBZ). Data collected on 3 May 1978 from 0216 GMT to 0233 GMT.

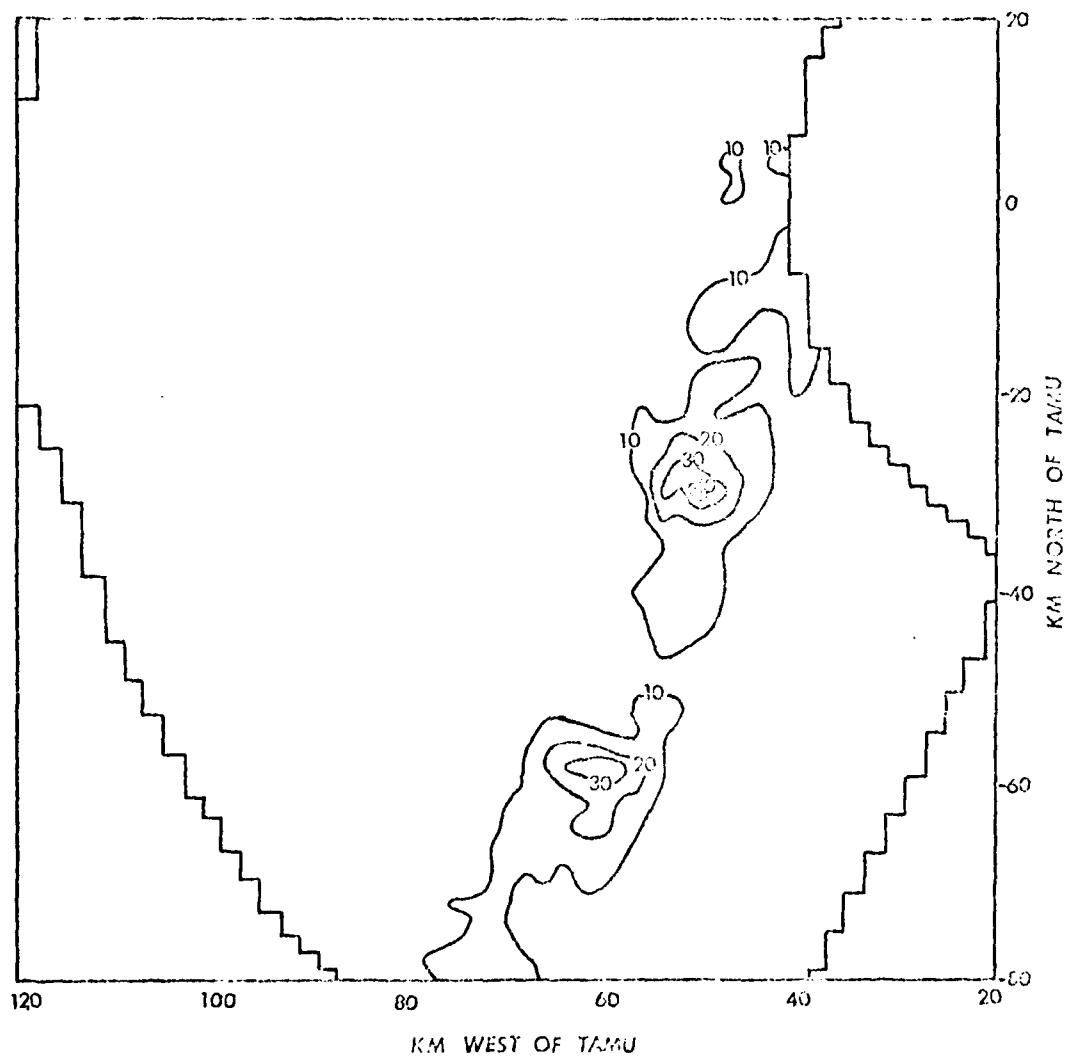


Fig. 15. Tilt-sequence ten, southwest sector, VIL (kg m^{-2}).
Data collected on 3 May 1978 from 0216 GMT to 0233 GMT.

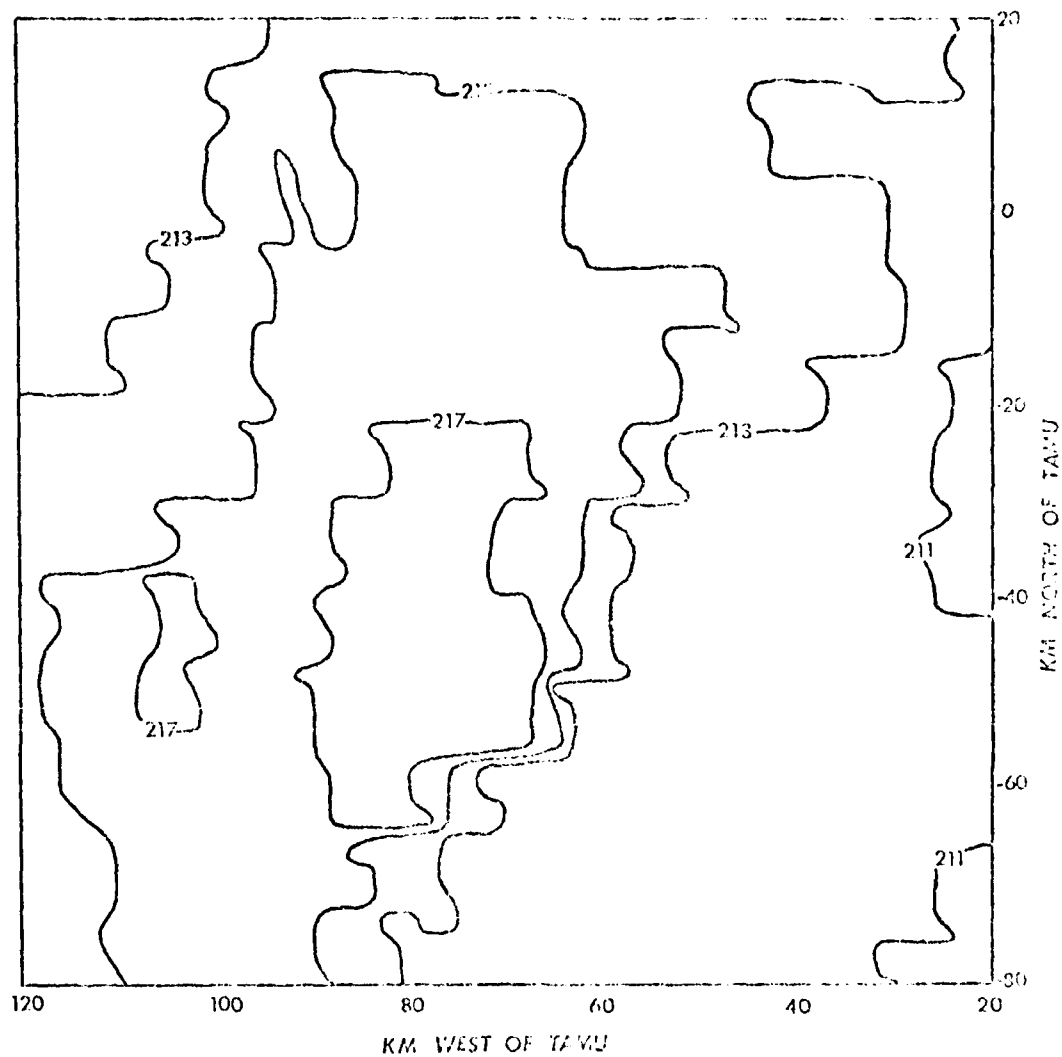


Fig. 16. 0215 GMT, 3 May 1978 infrared image, southwest sector.

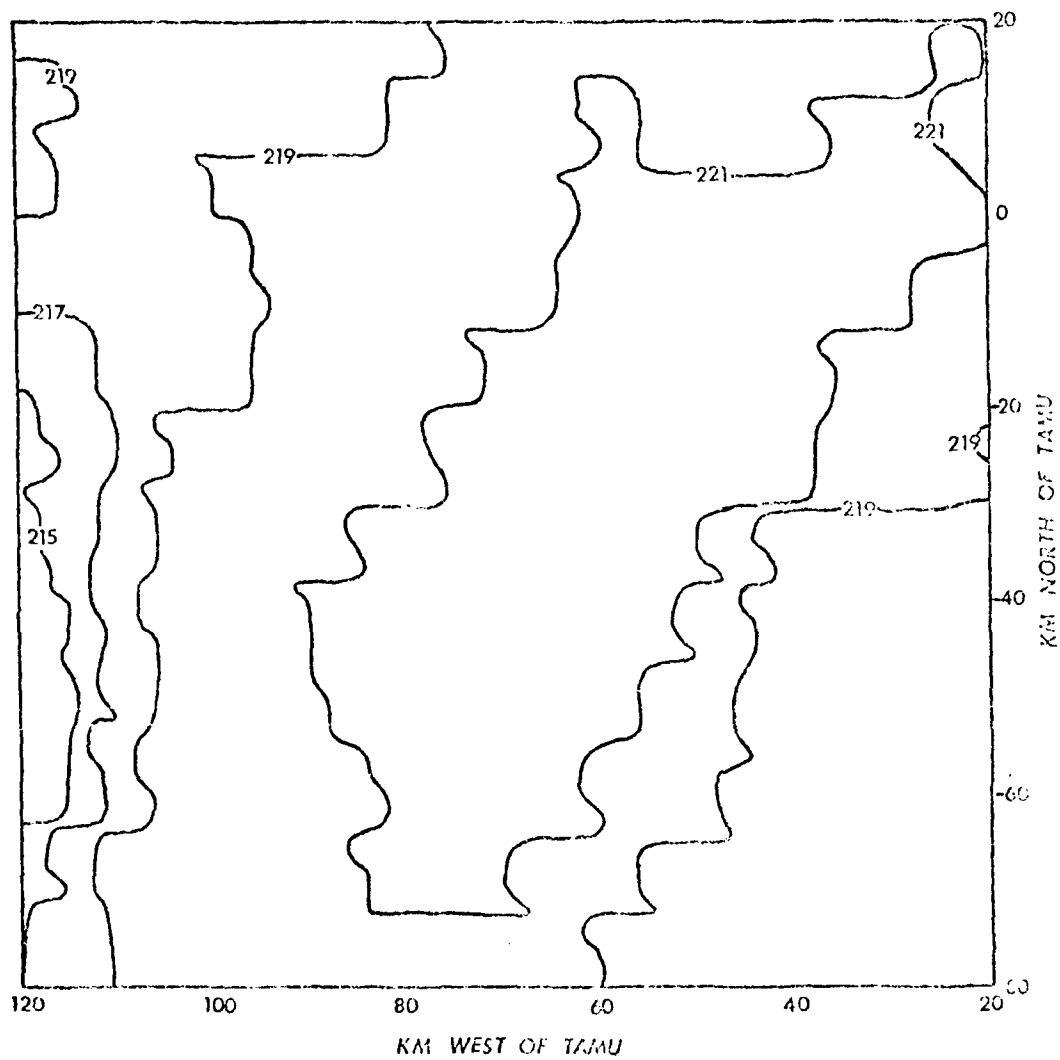


Fig. 17. 0230 GMT, 3 May 1978 infrared image, southwest sector.

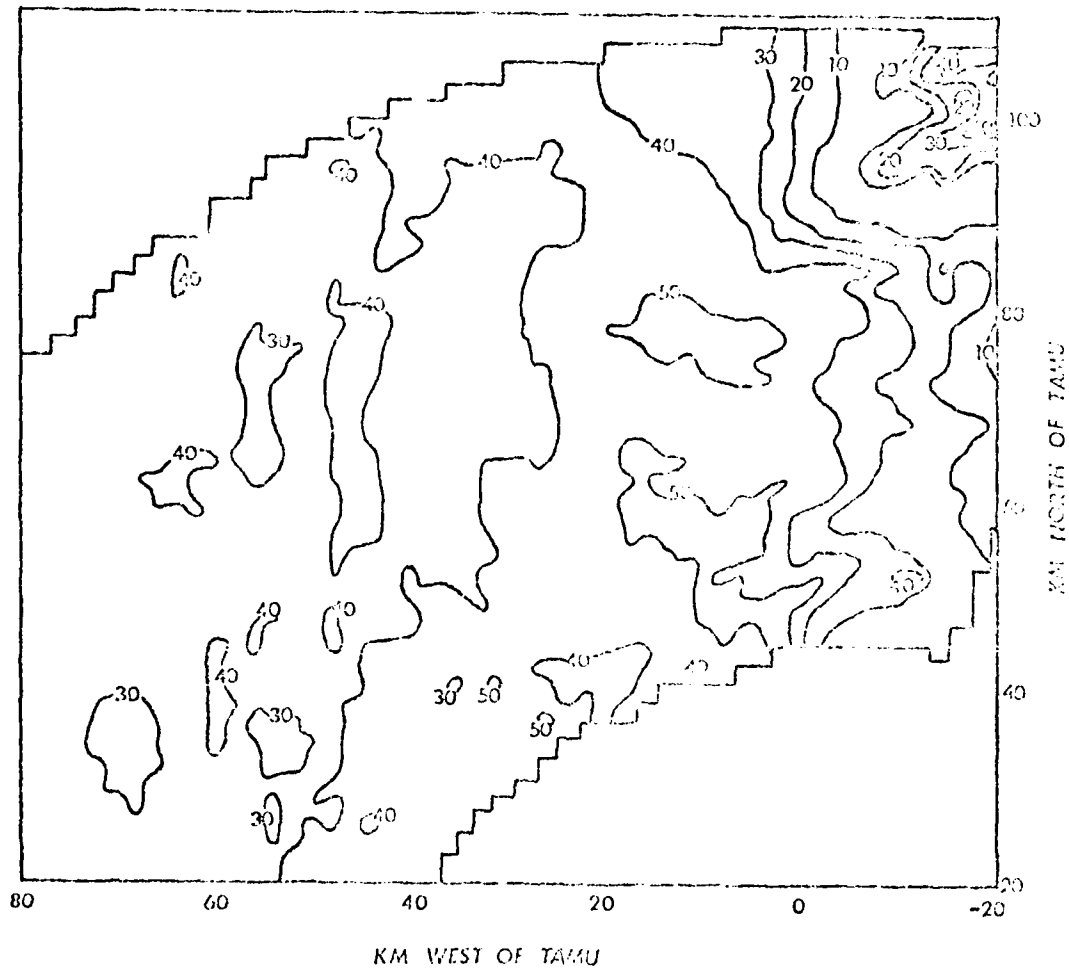


Fig. 18. Tilt-sequence ten, northwest sector, zero-tilt reflectivity (dBZ). Data collected on 3 May 1978 at 0216 GMT.

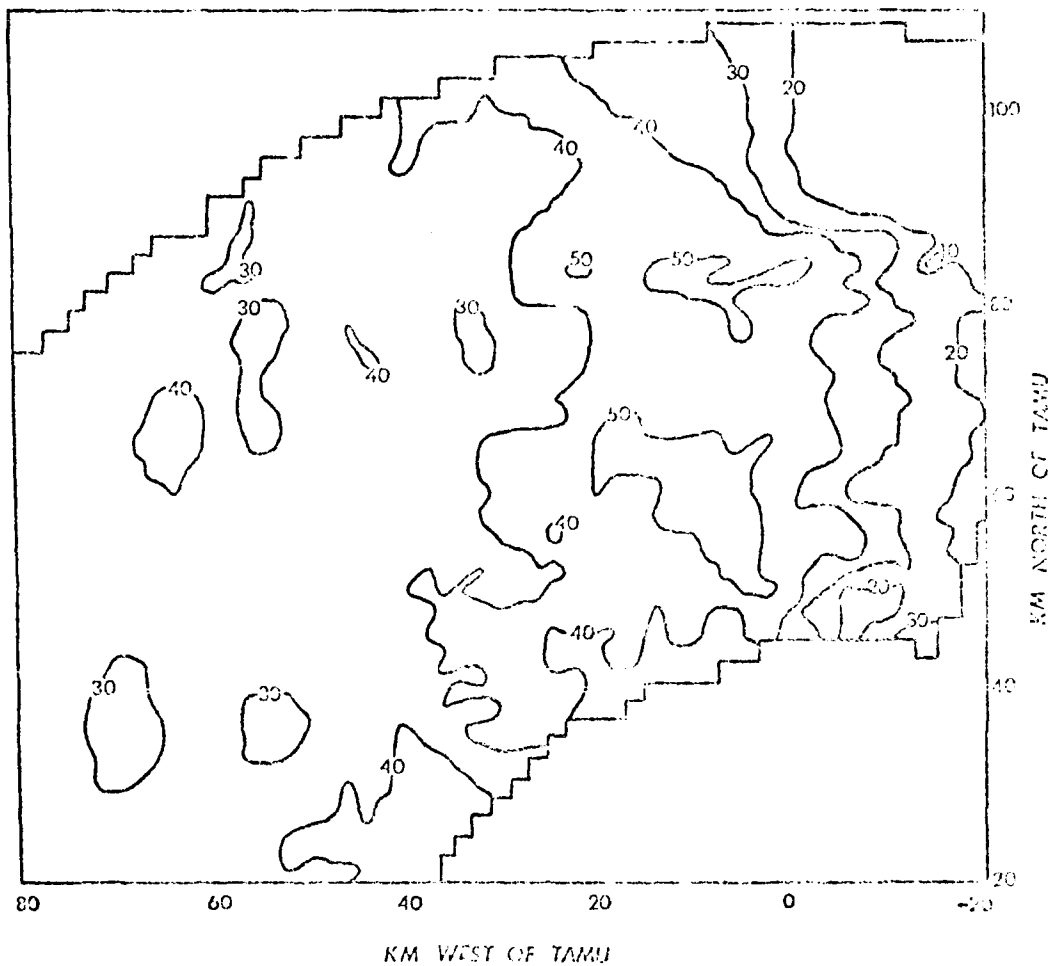


Fig. 19. Tilt-sequence ten, northwest sector, low-level PVSZ (dBZ). Data collected on 3 May 1978 from 0216 GMT to 0233 GMT.

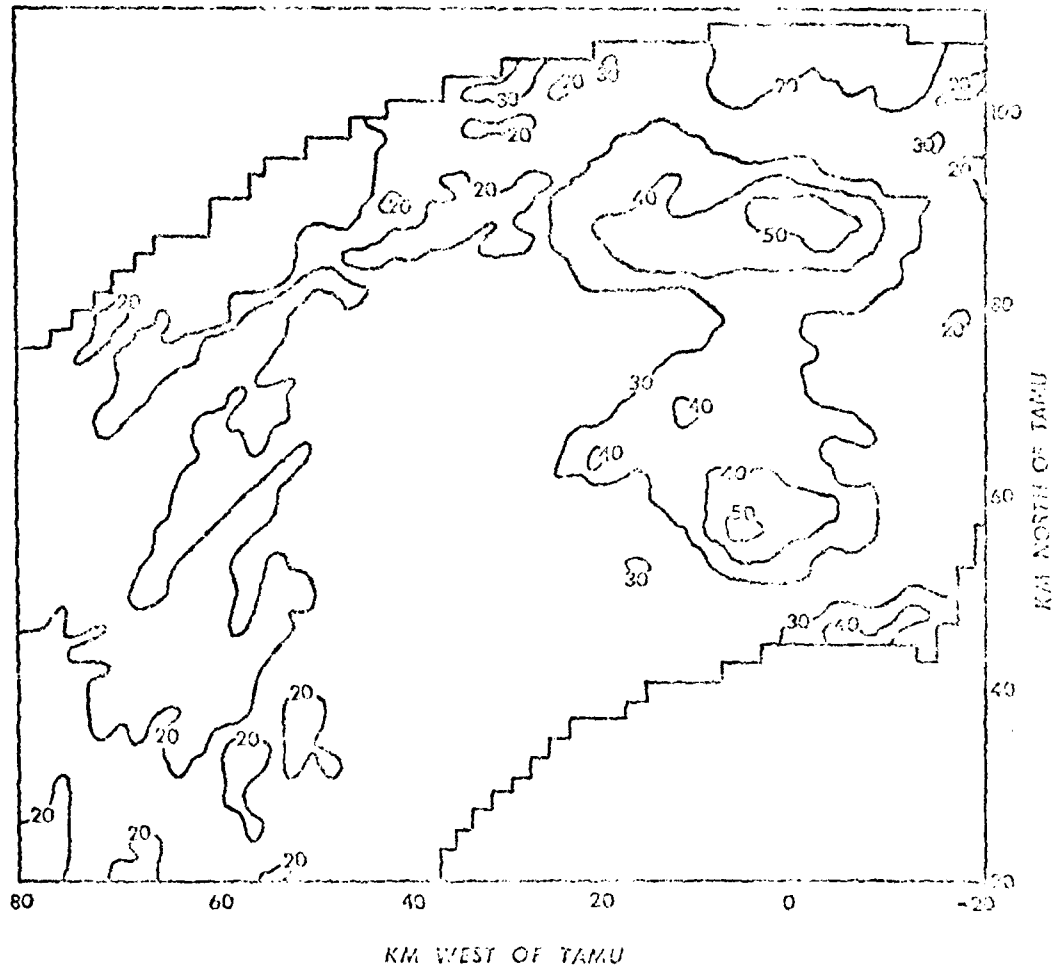


Fig. 20. Tilt-sequence ten, northwest sector, mid-level PVSZ (dBZ). Data collected on 3 May 1978 from 0216 GMT to 0233 GMT.

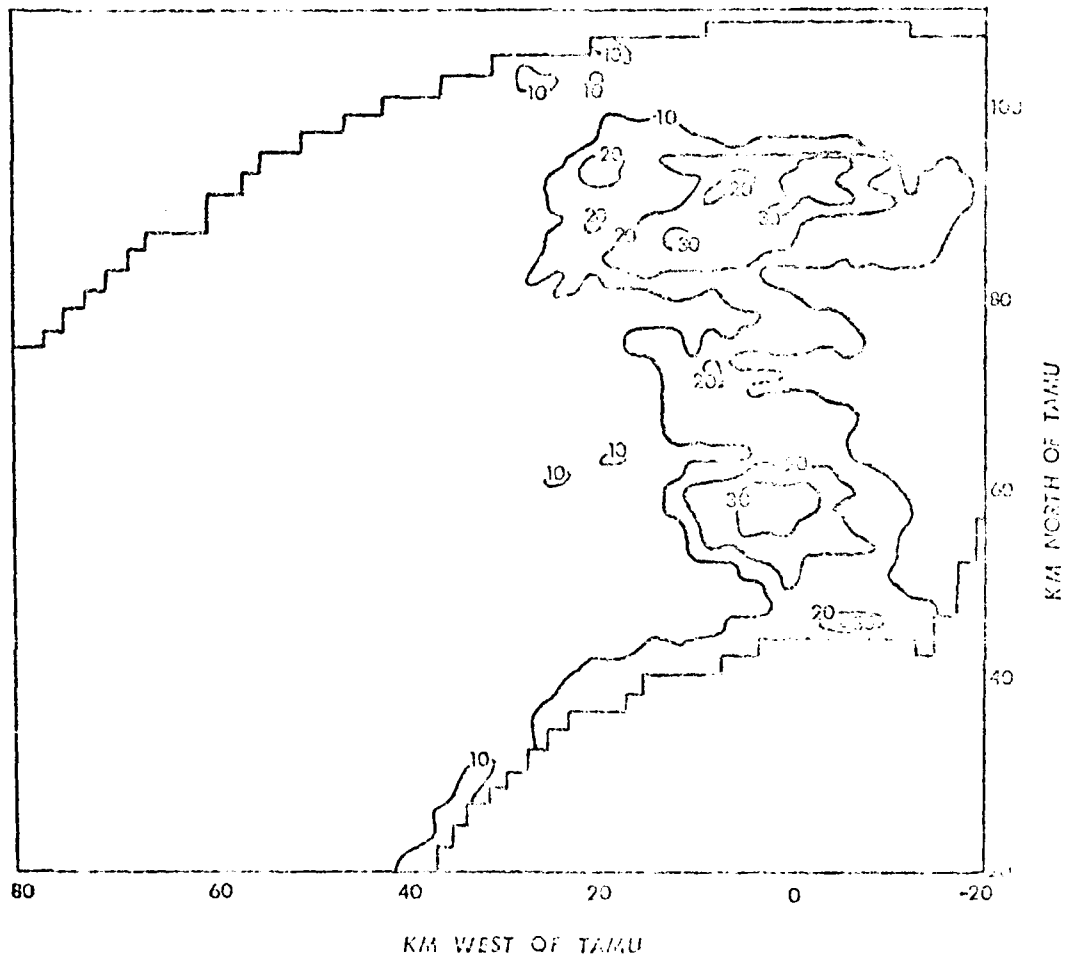


Fig. 21. Tilt-sequence ten, northwest sector, upper-level PVSZ (dBZ). Data collected on 3 May 1978 from 0216 GMT to 0233 GMT.

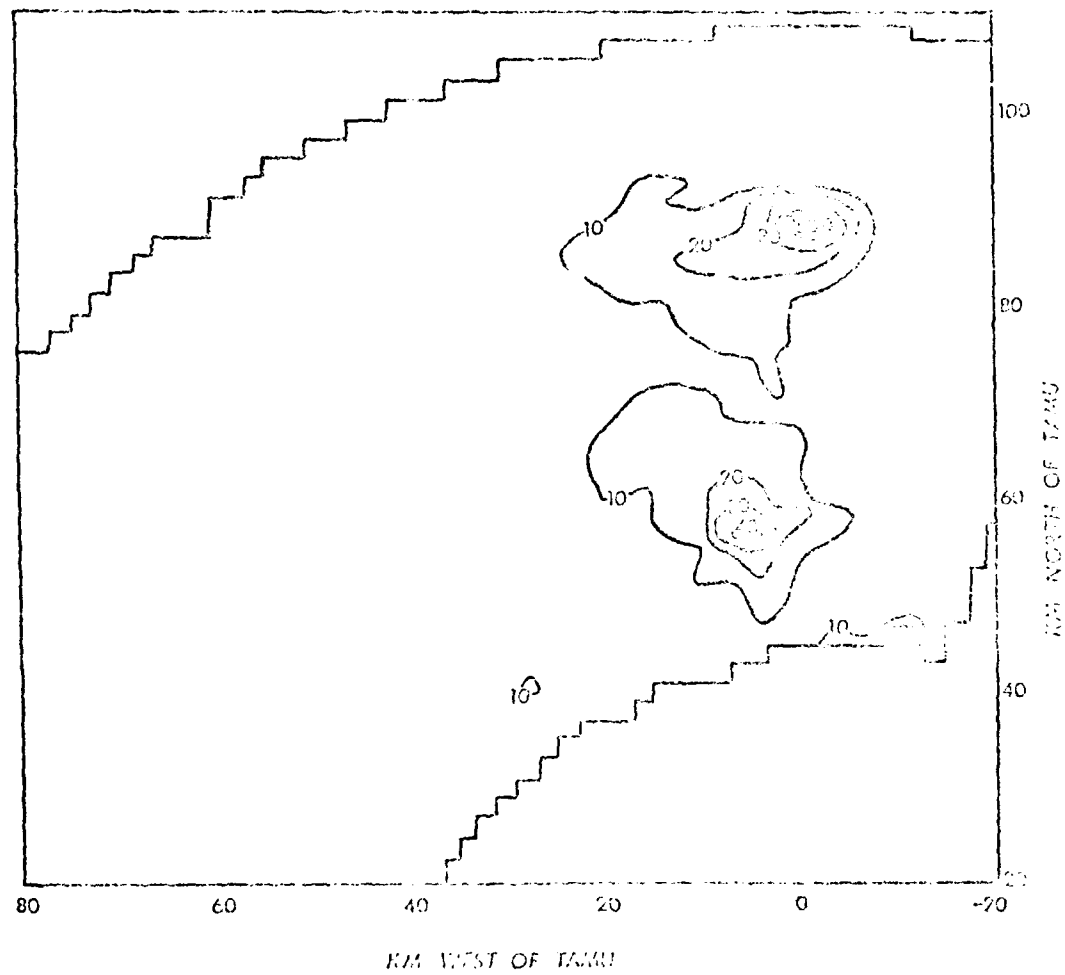


Fig. 22. Tilt-sequence ion, northwest sector, VIL (kg m^{-2}).
Data collected on 3 May 1978 from 0216 GMT to 0233 GMT.

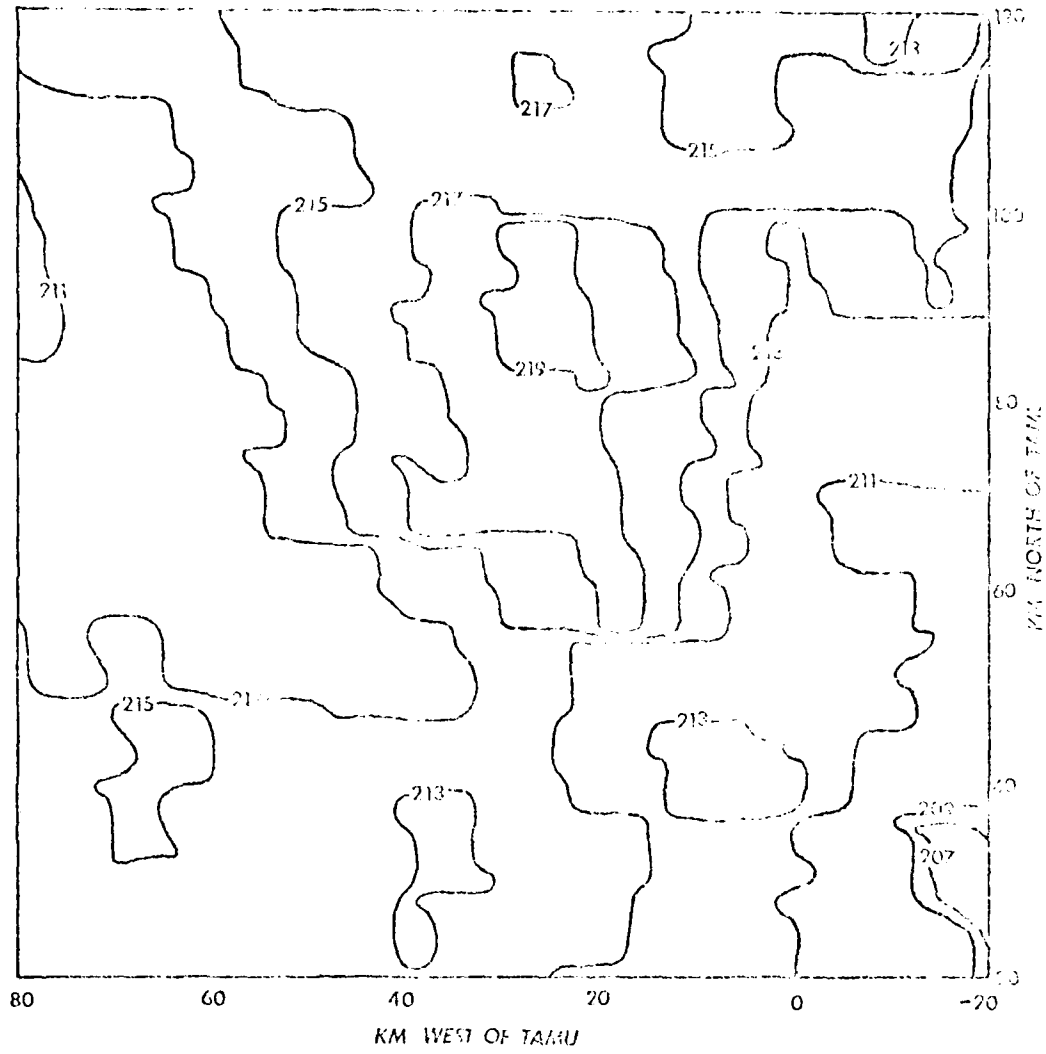


Fig. 23. 0215 GMT, 3 May 1978 infrared image, northwest sector.

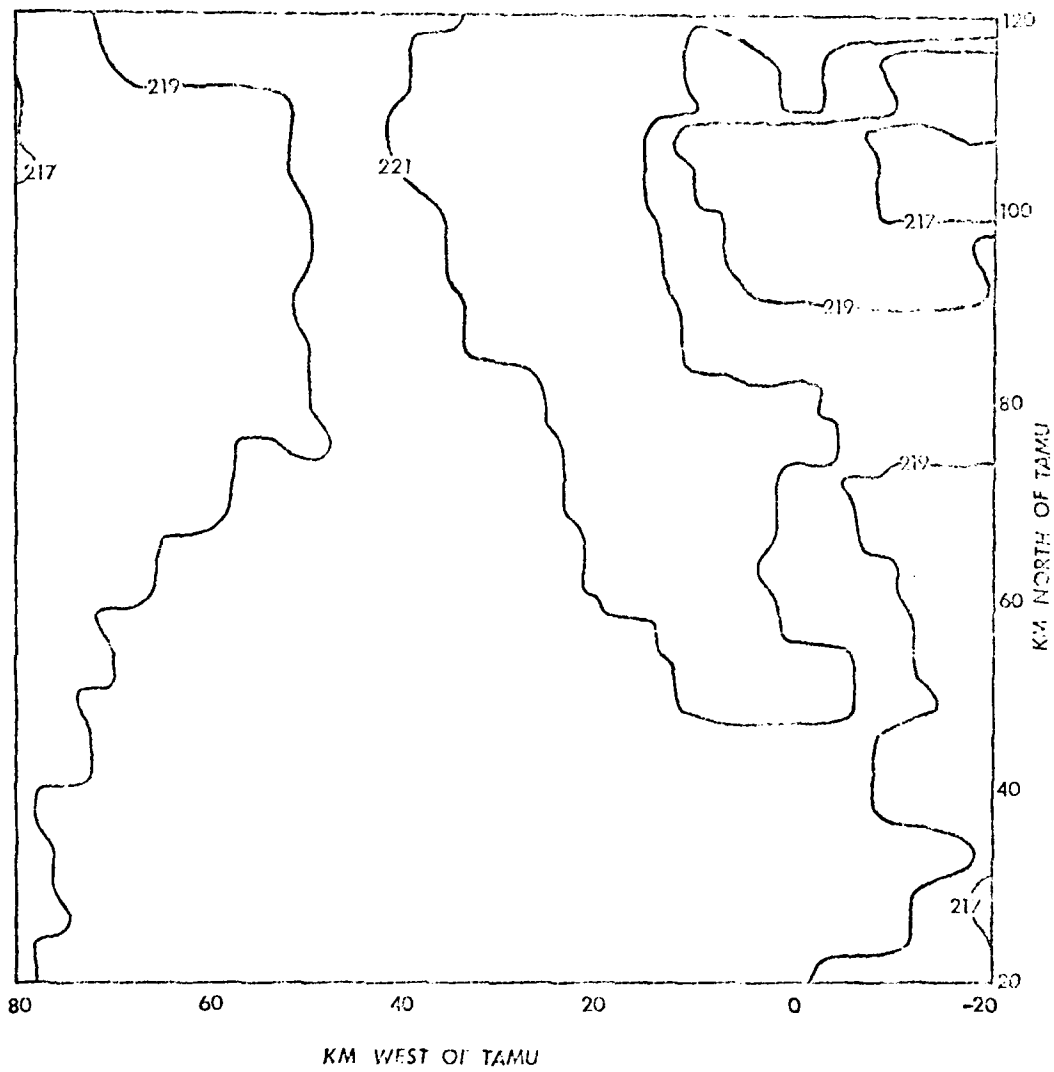


Fig. 24. 0230 GMT, 3 May 1978 infrared image, northwest sector.

with the location of reflectivity maxima in these same figures.

High values of infrared digital count in both the 0215 GMT and 0230 GMT images (Figs. 16 and 17) lie some 10 km to the west-northwest of radar activity indicated in Figs. 11 through 15. The increase in maximum digital count in going from the 0215 GMT image to the 0230 GMT image is indicative of the strong upper-level outflow associated with the line of convective activity. Regions of maximum digital count in both images lie overlap the maxima in the radar fields, especially in the later infrared image (Fig. 17).

b. Northwest Sector

Strong echo activity is also evident in the radar data for the northwest sector. Strong echoes are present to the north of TAMU with cells in the line activity becoming more evident in the mid- and upper-level PWSZ maps (Figs. 20 and 21). Two cells stand out very well in the VIL map (Fig. 22). Very little tilt is evident in the cells to the north of TAMU although the area of reflectivity associated with each cell in Figs. 19 through 21 is broader with merging of the cells apparently occurring at all levels. The VIL map (Fig. 22) exhibits two sharply bounded cells almost due north of TAMU.

Maximum values of digital count in the 0215 GMT infrared image (Fig. 23) lie 10-15 km to the west of maxima in the radar maps.

Maximum values of digital count in the 0230 GMT infrared image lie slightly to the west of maxima in the digital radar fields. The increase in maximum digital count from 0215 GMT to 0230 GMT again indicates the strong upper-level outflow associated with the convective line.

4. Correlations Between the Radar and Satellite Data

Correlation analysis provides a measure of the degree of association between variables. The correlation used as a measure of association in the remainder of this investigation is Pearson's product-moment correlation with the correlation coefficient, r , being given by

$$r = \frac{\sum_{i=1}^N (X_i - \bar{X})(Y_i - \bar{Y})}{\left[\sum_{i=1}^N (X_i - \bar{X})^2 \sum_{i=1}^N (Y_i - \bar{Y})^2 \right]^{0.5}} \quad (1)$$

where the (X_i, Y_i) represent paired observations of the variables, \bar{X} and \bar{Y} represent arithmetic means of the variables, and N is the total number of paired observations of X and Y . The value of the coefficient, r , is a measure of the degree of association of the variables with a perfect positive association indicated by $r = 1$, a perfect negative correlation indicated by $r = -1$, and a complete lack of correlation between the variables indicated by $r = 0$.

Correlation coefficients were computed using procedures implemented by the SAS 76 statistical analysis system which also returned significance probabilities of the correlation coefficients. The significance probability, p , of a correlation coefficient is the probability that a value of the correlation coefficient as large or larger in absolute value than the one calculated would have arisen by chance were the two random variables truly uncorrelated (Bar et al., 1976). Correlation coefficients were calculated for three basic data sets: the first tilt-sequence and associated GOES images, the tenth tilt-sequence, southwest sector, and associated GOES images, and the tenth tilt-sequence, northwest sector, and associated images. All values of r were computed using point values of the radar and satellite variables.

An additional satellite data variable was artificially created for each data set by subtracting point values of the digital count of the later GOES image from corresponding values of digital count in the earlier GOES image. Correlation coefficients also were computed between this difference in digital count, d , and the digital radar data.

a. First Tilt-sequence and Corresponding GOES Images

The results of the correlations of the 0015 GMT infrared data, the 0030 GMT infrared data, and d with corresponding digital radar data are tabulated in Table 3. The best correlations were found

Table 3. Values of r and p for the first tilt-sequence and corresponding CORIS images.

Satellite Data	Radar Data	r	p
0015 GMT Image	Zero-tilt reflectivity	-0.177	0.0001
	Low-level PWSZ	-0.058	0.0004
	Mid-level PWSZ	0.372	0.0001
	Upper-level PWSZ	0.105	0.0001
	VIL	0.123	0.0001
0030 GMT Image	Zero-tilt reflectivity	0.019	0.3937
	Low-level PWSZ	0.120	0.0001
	Mid-level PWSZ	0.496	0.0001
	Upper-level PWSZ	0.184	0.0001
	VIL	0.247	0.0001
Difference, d	Zero-tilt reflectivity	0.216	0.0001
	Low-level PWSZ	0.105	0.0001
	Mid-level PWSZ	-0.205	0.0001
	Upper-level PWSZ	-0.070	0.0005
	VIL	-0.079	0.0003

Number of Observations = 2000

between the 0015 GMT and 0030 GMT images and mid-level PVSZ data. Weak and sometimes negative correlation coefficients were found between both infrared images and zero-tilt reflectivity and low-level PVSZ. Weak positive correlations are indicated for both images and upper-level PVSZ and VIL. The results for the point differences in digital counts between images and the radar data are ambiguous with a weak positive correlation between d and zero-tilt reflectivity and low-level PVSZ and negative correlations with the remaining radar data fields.

b. Tenth Tilt-sequence, Southwest Sector, and Corresponding GOES Images

The results of correlations of the 0215 GMT infrared data, the 0230 GMT infrared data, and d with the corresponding digital radar data from the southwest sector of the tenth tilt-sequence are tabulated in Table 4. The best correlations in this data set were between a mid-level and upper-level PVSZ and d , the difference between digital counts for the 0230 GMT and 0215 GMT images. Fair positive correlations also were found between d and VIL and between the 0230 GMT image and zero-tilt reflectivity and low-level PVSZ. Somewhat weaker correlations were found between the 0230 GMT image and mid- and upper-level PVSZ and VIL. Weak positive correlations were found between the 0215 GMT image and zero-tilt reflectivity and low-level

Table 4. Values of r and p for the tenth tilt-sequence and corresponding GOES images (southwest sector).

Satellite Data	Radar Data	r	p
0215 GMT Image	Zero-tilt reflectivity	0.317	0.0001
	Low-level PVSZ	0.332	0.0001
	Mid-level PVSZ	-0.244	0.0001
	Upper-level PVSZ	-0.399	0.0001
	VIL	-0.221	0.0001
0230 GMT Image	Zero-tilt reflectivity	0.544	0.0001
	Low-level PVSZ	0.530	0.0001
	Mid-level PVSZ	0.389	0.0001
	Upper-level PVSZ	0.275	0.0001
	VIL	0.401	0.0001
Difference, d	Zero-tilt reflectivity	0.063	0.0050
	Low-level PVSZ	0.037	0.1034
	Mid-level PVSZ	0.648	0.0001
	Upper-level PVSZ	0.624	0.0001
	VIL	0.527	0.0001

Number of Observations = 1986

PVSZ. Negative correlations existed between the 0215 GMT image and mid-level and upper-level IVSZ and VII. Zero-tilt reflectivity and low-level PVSZ were essentially uncorrelated with d.

c. Tenth Tilt-sequence, Northwest Sector, and Corresponding GOES Images

Table 5 lists the results of correlations of 0215 GMT infrared data, 0230 GMT infrared data, and d with the corresponding digital radar data from the northwest sector of the tenth tilt-sequence. The best correlations in this data set were between the 0230 GMT infrared data and zero-tilt reflectivity and low-level PVSZ. Weaker positive correlations were found between the 0230 GMT infrared data and the remaining digital radar fields. Correlations were also found for the digital radar field, while positive and significant, values were also found for the same data fields in the southeast sector. Except for weak positive correlations between the 0215 GMT infrared data and zero-tilt reflectivity and low-level PVSZ, the 0215 GMT infrared data were uncorrelated with the digital radar data.

5. The Effect of Thresholding the Data

Enhanced infrared imagery from meteorological satellites has proved useful in detecting the presence of severe convective activity, in examining the structure of convective storm systems, and in estimating the amount of precipitation from convective storm systems.

Table 5. Values of r and p for the tenth tilt-sequence and corresponding GOES images (northwest sector).

Satellite Data	Radar Data	r	p
0215 CMT Image	Zero-tilt reflectivity	0.188	0.0001
	Low-level PVSZ	0.167	0.0001
	Mid-level PVSZ	-0.014	0.5557
	Upper-level PVSZ	-0.091	0.0001
	VIL	0.008	0.7559
0230 CMT Image	Zero-tilt reflectivity	0.598	0.0001
	Low-level PVSZ	0.592	0.0001
	Mid-level PVSZ	0.373	0.0001
	Upper-level PVSZ	0.225	0.0001
	VIL	0.387	0.0001
Difference, d	Zero-tilt reflectivity	0.179	0.0001
	Low-level PVSZ	0.195	0.0001
	Mid-level PVSZ	0.246	0.0001
	Upper-level PVSZ	0.270	0.0001
	VIL	0.232	0.0001
Number of Observations = 1721			

Enhancing infrared images requires selecting various "thresholds" in the data and assigning various shades of grey in the "grey scale" to data bounded by the thresholds. These thresholds may then be used to produce patterns in the infrared data characteristic of various stages in the development of phenomena such as hurricanes and squall lines.

An example of an enhancement applied to infrared imagery is the MB enhancement curve shown in Fig. 25 and tabulated in Table 6. The MB enhancement is applied to GOES infrared imagery as a means of delineating areas of thunderstorm activity in the images. The very cold tops typically associated with areas of intense convective activity are thresholded in the grey scale as areas of dark and black tones seen against the lighter background of lower-level, warmer clouds in the hard copy imagery. A reversal of the scale from black to white is used to identify the strongly penetrative tops indicative of severe thunderstorm activity (Cerbasi *et al.*, 1976).

a. Thresholding the Infrared Data

Selected digital count thresholds corresponding to levels employed in the MB enhancement curve were applied to the data used in this investigation. All infrared data having digital counts less than the threshold digital count and corresponding radar data were excluded from that step in the analysis. Due to the limited range of

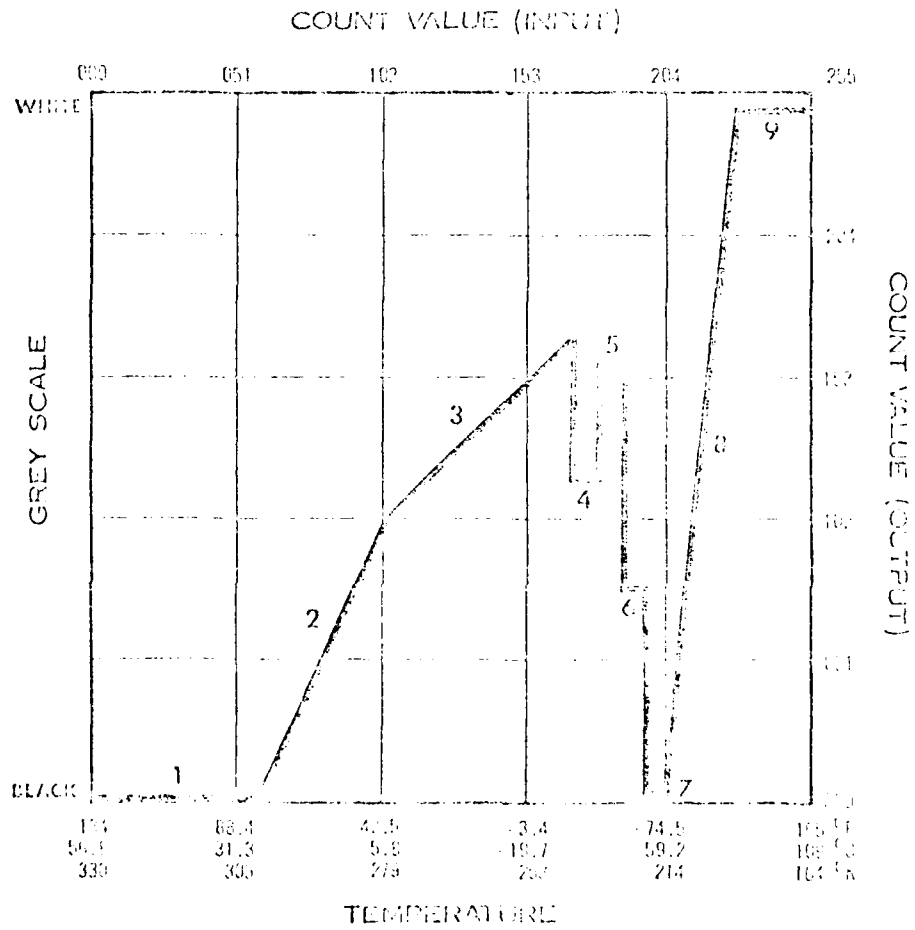


Fig. 25. MB enhancement curve (after Corbell *et al.*, 1976).

Table 6. MB enhancement (after Corbell et al., 1975).

Digital Count Threshold	Temperature (K)	Remarks (Grey Scale Shade)
057	301.5	Low level/sea surface difference
100	280.0	Middle level - no enhancement
177	241.0	First level of sea (Medium grey)
187	231.0	Thunderstorm enhancement (Light grey)
198	220.0	Thunderstorm enhancement (Dark grey)
204	214.0	Thunderstorm enhancement (Black)
208	210.0	Overexposed tops enhancement (White)
226	192.0	

digital count values associated with the portions of the 0215 GMT and 0230 GMT infrared images used and the high values of digital count in the images, the data for the tenth tilt-sequence and corresponding infrared data were excluded from this portion of the analysis. The remaining data set, the first tilt-sequence and 0015 GMT and 0030 GMT infrared images, was examined using a threshold value of infrared digital count. Table 7 presents the correlation coefficients resulting from the correlation of thresholded infrared data with corresponding digital radar data.

Thresholding the 0015 GMT infrared image improved the correlation between the image data and the digital radar data for threshold digital counts of 187 and 198. The correlations between infrared image data and all radar data except upper-level PVSZ were markedly improved when the 198 digital count threshold was evaluated. Increasing the threshold digital count for this image to 204 worsened the correlation, possibly due to reduced sample size as well as other factors. Thresholding the 0030 GMT results produced similar results for the 193 digital count threshold in that all correlations were somewhat improved. The 204 and 206 digital count thresholds improved correlations with zero-tilt reflectivity and low-level PVSZ while the correlation with mid-level PVSZ diminished. The correlation with upper-level PVSZ remained essentially the same.

AD-A110 365

AIR FORCE INST OF TECH WRIGHT-PATTERSON AFB OH

F/6 4/2

DIGITAL METEOROLOGICAL RADAR DATA COMPARED WITH DIGITAL INFRARE--ETC(U)

MAY 79 R S HENDERSON

AFIT-CI-79-278T-5

NL

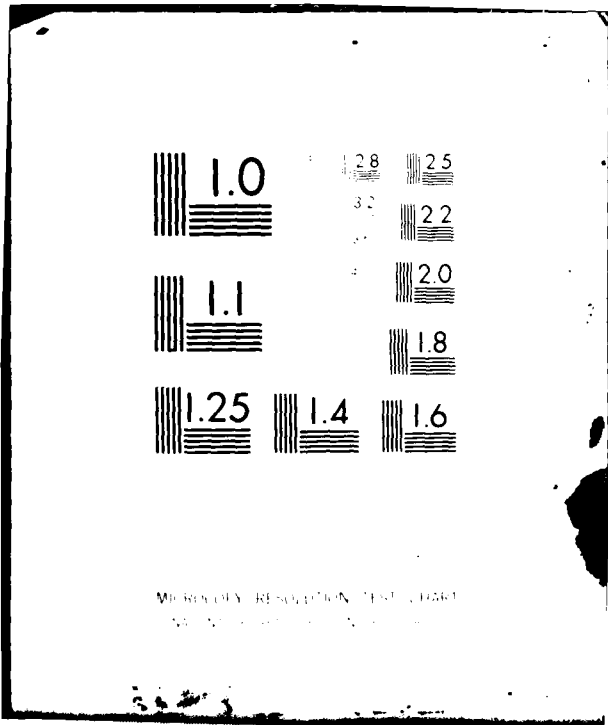
UNCLASSIFIED

2 of 2

AD-A
100-100

1

END
DATE
FILMED
03-82
DTIC



MICROCOPY RESOLUTION TEST CHART
NBS 1010A

Table 7. Values of r and p for the first tilt-sequence and thresholded GOES images.

Digital Count Threshold	Infrared Image Time (GMT)	Radar Data	r	p	Number of Observations
187	0015	Zero-tilt reflectivity	0.109	0.0001	1382
		Low-level PVSZ	0.121	0.0001	
		Mid-level PVSZ	0.141	0.0001	
		Upper-level PVSZ	0.121	0.0001	
		VIL	0.233	0.0001	
198	0030	Zero-tilt reflectivity	0.019	0.3937	2061
		Low-level PVSZ	0.120	0.0001	
		Mid-level PVSZ	0.195	0.0001	
		Upper-level PVSZ	0.184	0.0001	
		VIL	0.247	0.0001	
187	0015	Zero-tilt reflectivity	0.476	0.0001	1323
		Low-level PVSZ	0.454	0.0001	
		Mid-level PVSZ	0.520	0.0001	
		Upper-level PVSZ	0.167	0.0001	
		VIL	0.398	0.0001	
198	0030	Zero-tilt reflectivity	0.036	0.0822	2052
		Low-level PVSZ	0.131	0.0001	
		Mid-level PVSZ	0.500	0.0001	
		Upper-level PVSZ	0.180	0.0001	
		VIL	0.247	0.0001	

Table 7. (Continued.)

Digital Count Threshold	Infrared Image Time (GMT)	Radar Data	r	p	Number of Observations
198	0030	VIL	0.255	0.0001	2052
204	0015	Zero-tilt reflectivity	0.448	0.0001	505
		Low-level PVSZ	0.335	0.0001	
		Mid-level PVSZ	0.197	0.0001	
		Upper-level PVSZ	0.055	0.1002	
		VIL	0.259	0.0001	
	0030	Zero-tilt reflectivity	0.176	0.0001	1675
		Low-level PVSZ	0.192	0.0001	
		Mid-level PVSZ	0.339	0.0001	
		Upper-level PVSZ	0.197	0.0001	
		VIL	0.251	0.0001	
208	0015	Zero-tilt reflectivity	-0.494	0.0002	53
		Low-level PVSZ	-0.673	0.0001	
		Mid-level PVSZ	-0.551	0.0001	
		Upper-level PVSZ	-0.113	0.4207	
		VIL	-0.544	0.0001	
	0030	Zero-tilt reflectivity	0.305	0.0001	343
		Low-level PVSZ	0.385	0.0001	
		Mid-level PVSZ	0.281	0.0001	
		Upper-level PVSZ	0.143	0.6032	
		VIL	0.395	0.0001	

the thresholding process. The correlation with VIL was generally improved by the thresholding process with the best correlation at digital counts at and above 208.

b. Thresholding the Digital Radar Data

The thresholding process was extended to the digital radar data as well and correlation coefficients were computed between the radar and satellite data. The initial thresholding was performed by examining only radar data with nonzero values for the variables. In a few isolated cases a slight improvement in correlations between the satellite data and zero-tilt reflectivity was observed. In all other cases the correlation was diminished, markedly so in some instances.

To examine further the effect of thresholding the digital radar data, arbitrary thresholds were selected and correlation coefficients computed between the radar and satellite data. Threshold levels of 10 dBZ were selected for zero-tilt reflectivity, low-level PVSZ, and mid-level PVSZ data. A threshold level of 5 dBZ was selected for the upper level PVSZ data and of 5 kg m^{-2} for the VIL data. Correlation coefficients computed for the thresholded radar data and corresponding infrared images are listed in Table 8.

Thresholding the radar data in the first tilt-sequence improved the correlation between zero-tilt reflectivity, low-level PVSZ, and mid-level PVSZ and both infrared images. No improvement was

Table 8. Values of r and p for thresholded radar data and GOES images.

Tilt-sequence	Infrared Data	Radar Data	r	p	Number of Observations
First Southwest Sector	0015 GMT Image	Zero-tilt reflectivity	0.072	0.0136	1186
		Low-level PWSZ	0.299	0.0001	1173
		Mid-level PWSZ	0.247	0.0001	1311
		Upper-level PWSZ	0.293	0.0257	53
	VIL	0.081	0.5009	72	
	0030 GMT Image	Zero-tilt reflectivity	0.142	0.0001	1165
		Low-level PWSZ	0.356	0.0001	1173
		Mid-level PWSZ	0.310	0.0001	1311
		Upper-level PWSZ	0.397	0.0010	53
	VIL	-0.123	0.3022	72	
Difference, d	Zero-tilt reflectivity	-0.049	0.0923	1196	
	Low-level PWSZ	-0.266	0.0601	1173	
	Mid-level PWSZ	-0.206	0.0001	1311	
	Upper-level PWSZ	-0.201	0.1307	53	
VIL	0.032	0.749	72		
Tenth, Southwest Sector	0215 GMT Image	Zero-tilt reflectivity	0.039	0.1073	1841
		Low-level PWSZ	0.155	0.0001	1860
		Mid-level PWSZ	-0.357	0.0001	1968
		Upper-level PWSZ	-0.304	0.0001	724
	VIL	-0.301	0.0001	433	
	0230 GMT Image	Zero-tilt reflectivity	0.500	0.0001	1841
		Low-level PWSZ	0.434	0.0001	1860

Table 8. (Continued)

Tilt-sequence	Infrared Data	Radar Data	r	p	Number of Observations
Tenth, Southwest Sector	0230 GMT	Mid-level	0.367	0.0001	1958
	Image	Upper-level	0.092	0.0131	724
		VIL	0.117	0.0150	433
Difference, d	Zero-tilt reflectivity		0.314	0.0001	1841
	Low-level PWSZ		0.192	0.0001	1660
	Mid-level PWSZ		0.647	0.0001	1969
	Upper-level PWSZ		0.452	0.0001	724
	VIL		0.406	0.0001	433
Tenth, Northwest Sector	0215 GMT	Zero-tilt reflectivity	0.261	0.0001	1663
	Image	Low-level PWSZ	0.222	0.0001	1684
		Mid-level PWSZ	-0.014	0.5557	1721
		Upper-level PWSZ	-0.023	0.5628	601
		VIL	-0.130	0.0005	475
0230 GMT	Zero-tilt reflectivity		0.603	0.0001	1663
	Image	Low-level PWSZ	0.567	0.0001	1684
		Mid-level PWSZ	0.873	0.0001	1721
		Upper-level PWSZ	0.919	0.0002	601
		VIL	0.006	0.8099	475
Difference, d	Zero-tilt reflectivity		0.098	0.0001	1663
	Low-level		0.116	0.0001	1684
	Mid-level		0.245	0.0001	1721
	Upper-level		0.035	0.2541	601
	VIL		0.151	0.0010	475

obtained in the other correlations or for correlations of the radar data with d.

Thresholding the radar data in the southwest sector of the tenth tilt-sequence improved the correlation of d with zero-tilt reflectivity and low-level PVSZ but did not improve any other correlation in the data set. Thresholding the radar data in the northwest sector of the tilt-sequence improved the correlation of both infrared images with zero-tilt reflectivity and of the 0215 GMT image with low-level PVSZ. The remaining correlations were not improved by the thresholding process.

Simultaneous thresholding of both the digital radar and digital satellite data was not attempted since only data from the first tilt-sequence and corresponding imagery could have been used. Reduced sample size in such thresholding probably would have resulted in misleading or erroneous results, particularly for comparisons with upper-level PVSZ and VIL.

CHAPTER V

CONCLUSIONS AND RECOMMENDATIONS

1. Conclusions

The primary objective of this investigation was to compare digital meteorological radar data with infrared imagery from a meteorological satellite in geostationary orbit by determining the correlation between point values of infrared digital count and point values of radar reflectivity and vertically integrated liquid water content (VIL). Digital data from the 10 cm radar of the Department of Meteorology at TAMU were processed by a modified version of Sieland's (1977) computer program and displayed as output maps of point values of zero-tilt reflectivity, low-, mid-, and upper-level FVSZ, and VIL. Digital GOES-East infrared satellite data from McIDAS image save tapes were processed to produce maps of point values of infrared digital count mapped to the same projection and grid interval used for the digital radar data. The maps of digital radar and digital satellite images formed the basis for comparisons between the two types of data.

This investigation has led to the following conclusions:

- 1) Large-scale features evident in the digital radar data are also apparent in the infrared imagery. The obscuring of low and middle level convection by cirrus overcast and the different

resolutions of the infrared GOES imagery (~ 8 km) and the digital radar (~ 1 km interpolated to a 2-km grid spacing) make areas of weak convection that are apparent in the radar data difficult or impossible to locate in the infrared imagery. This problem is probably more important to rainfall-estimation efforts than to efforts to locate and measure the intensity of severe convective activity. The fair correlation between mid-level PVSZ and the infrared data in such an instance may provide a way to partially eliminate this problem, particularly when the infrared data are enhanced by thresholding.

2) Although only one set of 2061 observations could be examined, thresholding the infrared data significantly improved the correlation between the radar and satellite data, especially the correlation with zero-tilt reflectivity and low-level PVSZ. Cheng and Roderhals (1977) compared NOAA 2 infrared imagery with radar rainfall and determined that thresholding the satellite imagery did not improve the correlation. The results of this investigation suggest that thresholding the infrared GOES imagery should improve the correlation between the satellite data and radar rainfall. The difference in results may be due to procedural differences or to differences in the satellite sensors since the infrared sensor aboard the NOAA 2 satellite has a higher resolution than the GOES VISSR.

3) Correlations between the radar and satellite data, while

weak to fair, are in the main positive, and the correlation coefficients obtained suggest that the variability in one set of data is at least partially "explained by" the variability in the other set of data. As an example, a correlation coefficient of 0.5 suggests that 25 per cent of the variability in the dependent variable beyond its mean is explained by the independent variable. Correlation coefficients of the order of 0.4 to 0.6 were obtained in this study.

4) Thresholding the digital radar data improved correlations between the infrared images and zero-tilt reflectivity, low-level PVSZ, and mid-level PVSZ, thereby suggesting that such a procedure might be useful in situations where cirrus clouds are low and mid-level clouds are present. Caution must be exercised in such thresholding, however, since the correlation between the two types of data can be markedly diminished by this process if carried too far.

5) Thresholding the infrared imagery beyond a certain digital count diminishes the correlation between the infrared data and some of the radar data. The exact level at which this effect occurs was not determined in this study, but the results from the comparison of the first tilt-sequence with the infrared data suggest that thresholding above a digital count of 198 produces this effect with some of the digital radar variables and the infrared imagery. It is considered likely that a different enhancement than the MB curve used in this

investigation would produce better correlations of the data, since the MB curve is designed for use with hard copy imagery rather than digital data.

6) The resolution of the infrared data produced by the GOES VISSR is not sufficient to determine the strength of the correlation of infrared satellite data with digital radar data to the degree that might be desired. Given the results of Chang and Rodenhuis, who used a higher resolution sensor, the strength of the correlations obtained in this study is somewhat surprising and encouraging. The two investigations are not directly comparable, since Chang and Rodenhuis used radar rainfall derived from digital radar reflectivity in their analysis, but the results of this investigation suggest that a stronger relationship may exist between digital radar data and infrared satellite imagery than they discovered.

7) The best correlations between infrared images and radar data in the tenth tilt-sequence comparisons were obtained for the infrared image at the conclusion of the tilt-sequence, thus suggesting a significant time-dependence in comparisons of this type. Correlations between d and the digital radar data also indicate such a time-dependence.

2. Recommendations

The results of this investigation and its coincident review of the

literature in this area suggest the following recommendations concerning the comparison of digital radar and digital satellite imagery:

- 1) The TAMU Weather Radar System possesses a dual-wavelength capability that should be exploited in this type of investigation. Both 3-cm and 10-cm digital radar should be compared with infrared images of coincident times. Blended fields of radar data, obtained by sums, weighted sums, or functions of the 3-cm and 10-cm data, should be compared to the satellite imagery.

- 2) Smith and Reynolds (1976) have discussed digital combination of radar and satellite data for use in developing models of convective development, precipitation studies, and determining severe storm signatures. The relatively unique dual-wavelength capability of the TAMU digital weather radars should be exploited in studies of the type suggested by Smith and Reynolds by forming composites of the digital radar and digital satellite data. The blending of two different perspectives of the same storm system by combining the different types of data could shed new light on our understanding of convective processes and severe storm development.

- 3) The time-dependence in comparisons of digital satellite and digital radar data should be investigated to determine how great a difference can be tolerated before the correlations become too weak for valid analysis.

4) The remaining film sequences from the 3 May 1978 storm situation should be compared with corresponding GOES infrared imagery to examine the development of the fields and to confirm the correlation between the digital radar and digital satellite data.

5) The effect of thresholding the brightness data in comparisons of radar and satellite data needs further investigation.

6) A central computer program developed to process the digital radar and digital satellite data should be developed which will permit rapid and efficient comparison of the data fields.

7) Comparisons of visible satellite imagery and digital radar data should be accomplished to determine the degree of correlation between the data types and factors which may limit such correlation. Brightness normalization techniques should be developed to permit such correlations to be made even at transmission zenith angles and to facilitate comparisons between different sensors and different images.

8) A capability to navigate digital satellite imagery using basic satellite orbital data should be developed at TAMU to minimize dependence on outside sources for such support and to facilitate the use of data from many different sources. Such a capability is required for the efficient use of data sources such as the experimenter's tapes from the AOIPS (Atmospheric and Oceanic Information Processing System) (McKowan, 1977).

9) The time involved in this investigation suggests that more efficient utilization of resources can be obtained by using an interactive data handling system similar to the McIT² or the AOPES. Development of such a system at TAMU should be undertaken to enhance both the research and teaching capabilities within the College of Geosciences. The cost of developing such a system should be offset by maximizing the ability of such a system to handle different data fields from many different types of remote sensors and to broaden its applicability to include remote sensing problems in other academic disciplines while maintaining a basic orientation toward applications in meteorology and climatology.

REFERENCES

- Adler, R. F. and D. D. Fenn, 1977: Satellite-based thunderstorm intensity parameters. Preprints 10th Conf. on Severe Local Storms, Omaha, Amer. Meteor. Soc., 8-15.
- Barr, A. J., J. H. Goodnight, J. P. Sall, and J. T. Helvick, 1976: A User's Guide to SSM 75. SSM Institute, Raleigh, 329 pp.
- Barton, L. J., 1973: Radar Observation of the Air, University of Chicago, 324 pp.
- Blackmer, R. H., Jr., 1961: Satellite observations of squall line thunderstorms. Prep. 9th Pacific Meteor. Conf., Honolulu, Hawaii, Amer. Meteor. Soc., 76-82.
- _____, 1975: Correlation of cloud height and wind direction with precipitation intensity. Tech. Rpt. NEPA/CR 8-75 (S-3), Contract N00014-71-C-2350, Stanford Research Institute, 134 pp.
- _____, and S. M. Serebrany, 1969: Analysis of maritime precipitation using radar data and satellite global photographs. J. Appl. Meteor., 7, 122-131.
- Boucher, R. J., 1967: Relationships between the size of satellite-observed cirrus shields and the severity of thunderstorm complexes. J. Appl. Meteor., 6, 564-572.
- Cheng, N. and D. Rodenhuis, 1977: An intercomparison of satellite images and radar rainfall rates. Preprints 13th Technical Conf. on Hurricanes and Tropical Meteorology, Miami Beach, Amer. Meteor. Soc., 224-226.
- Corbell, R. P., C. J. Callahan, and W. J. Kotsch, 1976: The GOES/SMS User's Guide, National Environmental Satellite Service, Washington, 118 pp.
- Fujita, T. T., 1977: Meteorological satellite observations and army operations. Tech. Rpt. ECOM 77-6, University of Chicago, 37 pp.

- Gerrish, H. P., 1970: Satellite and radar analysis of mesoscale features in the tropics. Tech. Rpt. UCOM-0205-1, University of Miami, 45 pp.
- _____, 1975: Satellite and radar analysis of mesoscale weather systems. Tech. Rpt. UCOM-0014-1, University of Miami, 34 pp.
- Greene, D. R., 1971: Numerical techniques for the analysis of digital radar data with applications to meteorology and hydrology. Ph.D. dissertation, Texas A&M University, 124 pp.
- _____, 1964: An investigation of precipitation attenuation and its application in a dual-doppler frequency morphology of suboptical precipitation. M. S. thesis, Texas A&M University, 108 pp.
- Griffith, G. C. and W. L. Woodley, 1973: On the variation with height of the top brightness of precipitating convective clouds. J. Appl. Meteor., 12, 1086-1089.
- _____, W. L. Woodley, P. G. Grube, D. W. Martin, I. Stout, and D. N. Sikder, 1973: Rain estimation from geosynchronous satellite imagery - visible and infrared radiation. Ann. N.Y. Acad. Sci., 186, 1153-1171.
- Gruber, A., 1973: Estimating rainfall in regions of active convection. J. Appl. Meteor., 12, 110-118.
- Haig, T. O., 1978, Private communication.
- Haltiner, G. J., and F. L. Martin, 1957: Dynamical and Physical Meteorology. McGraw-Hill, New York, pp. 80-81.
- McAnelly, R. L., 1979: Private communication.
- McKowan, P. L., 1977: VISSR Data Processing Plan for Synchronous Meteorological and Geostationary Operational Environmental Satellites (SMS/GOES). NASA/Godard Space Flight Center, Greenbelt, 220 pp.
- Nagle, R. E., 1963: Comparisons of time integrated radar detected precipitation with satellite observed cloud patterns. Proc. 10th Radar Meteor. Conf., Washington, Amer. Meteor. Soc., 13-16.

- _____ and S. M. Serabry, 1962: Radar precipitation echo and satellite cloud observations of a maritime cyclone. J. Appl. Meteor., 1, 279-295.
- Negri, A. J., D. W. Reynolds, and R. A. Maddox, 1976: Measurements of cumulonimbus clouds using quantitative satellite and radar data. Proc. 7th Conf. on Numerical and Aerodynamic Meteor. and Symp. on Remote Sensing and Applications, 11-12, Amer. Meteor. Soc., 119-124.
- Noyland, M. A., 1978: An analysis of the data collection method of a digital weather radar system with respect to specific weather features. M. S. thesis, Texas A&M University, 146 pp.
- Phillips, J. H., 1975: Cloud structure from Defense Meteorological Satellite data. M. S. thesis, Texas A&M University, 100 pp.
- Robert-Jones, J. R., 1963: The radar equation for tilted clouds. Quart. J. Roy. Meteor. Soc., 88, 486-488.
- Reynolds, D. W., 1978: An intensive analysis of digital radar, rain-gage, and digital satellite data for a convective cloud system on the High Plains of Montana. Proceedings of Symp. on Meteorological Observations and Applications, 11-12, Denver, Amer. Meteor. Soc., 310-317.
- _____ and T. H. Vonder Haar, 1973: A comparison of radar-derived cloud height and reflected solar radiance measured from the geosynchronous satellite ATS-3. J. Appl. Meteor., 12, 1082-1086.
- _____, T. H. Vonder Haar, and L. O. Grant, 1978: Meteorological satellites in support of weather modification. Bull. Amer. Meteor. Soc., 59, 269-281.
- Sieland, T. E., 1977: Real-time computer techniques in the detection and analysis of severe storms from digital radar data. Ph. D. dissertation, Texas A&M University, 141 pp.
- Sikdar, D. N., 1972: ATS-3 observed cloud brightness field related to a meso-synoptic scale rainfall pattern. Tellus, 24, 400-413.
- Smith, E. A., 1975: The McIDAS system. IEEE Trans. Geosci. Electron., GE-13, 123-136.

- _____, and D. W. Reynolds, 1978: The generation and display of digital radar-satellite composites using analytic mapping techniques and solid state video refresh technology. Preprints Conf. on Wea. Forecasting and Analysis and Av. Res. Appl., Silver Spring, Amer. Meteor. Soc., 201-205.
- Vonder Haar, T. H., 1969: Meteorological applications of reflected radiance measurements from ATS 1 and ATS 3. J. Geophys. Res., 74, 5404-5412.
- _____, and R. S. Crum, 1970: A pilot study on the application of geosynchronous meteorological satellite data to very short range terminal forecasting. Tech. Rpt. AFGR-70-0428, Space Science and Engineering Center, University of Wisconsin, 116 pp.
- Weiss, C. H., 1978: Cloud-location correction in the horizon of an SMS image. Satellite Applications Information Note 78/3, National Environmental Satellite Service, Washington, 3 pp.
- Wexler, R. and E. J. Allison, 1972: Radar and Nimbus IV infrared measurements of the Oklahoma City tornadoes, 30 April 1973. Preprints 15th Radar Meteor. Conf., Champaign-Urbana, Amer. Meteor. Soc., 77-82.
- Young, J. T., 1978. Private communication.

APPENDIX A

THE MACMAP 3 AND MACIR COMPUTER PROGRAMS

This appendix contains copies of the MACMAP 3 and MACIR computer programs used to analyze the GOES images for this study.

VITA

Rodney B. Henderson was born in Fenwick, Georgia on 11 May, 1947, to Thomas Troy and Ann Henderson. After graduating from Campbell High School in 1965, he entered the Georgia Institute of Technology and graduated with a Bachelor of Science degree in geology degree in June 1970.

Rod was commissioned a 2nd Lt. in the Air Force in July 1970 and entered the Reserve Meteorology program at the University of Oklahoma on 12 September. Subsequent tour of duty included weather forecasting at Hamilton AFB, California, and four years of weather reconnaissance duty with the 54th and 53rd Weather Reconnaissance Squadrons at Anderson AFB and Keeler AFB, respectively. Rod also served as an augmentee to the 97th Weather Reconnaissance Group (Reserve) while stationed at Keeler AFB.

In September 1977 Rod entered Texas A&M University to pursue a Master of Science degree in Meteorology under Air Force Institute of Technology sponsorship. His permanent mailing address is in care of his sister at 2642 Highland Avenue, Smyrna, Georgia, 30080.

Rod Henderson is married to the former Sandra Leggins of Marietta, Georgia, and has two sons, Bryan and Jeremy.

3-8
DTIC